UNIVERSITY OF OKLAHOMA

GRADUATE COLLEGE

ANALYSIS OF POLARIMETRIC RADAR DOWNBURST PRECURSORS USING AUTOMATED STORM IDENTIFICATION AND TRACKING

A THESIS

SUBMITTED TO THE GRADUATE FACULTY

in partial fulfillment of the requirements for the

Degree of

MASTER OF SCIENCE

By

MACI NICOLE GIBSON
Norman, Oklahoma
2023

ANALYSIS OF POLARIMETRIC RADAR DOWNBURST PRECURSORS USING AUTOMATED STORM IDENTIFICATION AND TRACKING

A THESIS APPROVED FOR THE
SCHOOL OF METEOROLOGY

BY THE COMMITTEE CONSISTING OF

Dr. Guifu Zhang, Chair

Dr. Jacob Carlin

Dr. David Bodine

Dr. Pierre Emmanuel Kirstetter

Acknowledgements

I would first and foremost like to give the biggest thanks to my family, my friends, and my advisors whose never-ending support, advice, and encouragement allowed this project to thrive and made my graduate school experience so enjoyable. From the highs of getting to travel and present my work to the lows of overwhelming workloads, knowing that you all had my back is what got me to the end.

Thank you to my parents, my brother, and my grandparents who made sure I knew how proud you were of my accomplishments and were always willing to listen to my ramblings whether they involved complaining about code or the riveting dynamics of a storm happening miles away. A special thank you to my Papa, who always reminded me that he believed in me. You have all been there literally every step of the way, and I am forever grateful for that.

To my best friends here and across the country who helped me realize my full potential, who were happy to lend an ear or bit of advice to get me through the tough days, and who were ready to celebrate with me on the best days. Also to Figs and Sky, who provided lots of laughs and comforting cuddles (at their discretion, of course).

And to my advisors, Drs. Jacob Carlin and Guifu Zhang, and committee members, Drs. David Bodine and Pierre Kirstetter, whose guidance and help brought this research to life. Working with you all on this project provided me irreplaceable opportunities, and I am so excited and grateful that I get to present it.

TABLE OF CONTENTS

LIST OF TABLES

LIST OF FIGURES

Abstract

Strong thunderstorm winds produced by downbursts pose a threat to life, property, and aviation, yet they remain challenging to predict in advance. Current operational understanding of radar-based downburst precursors includes a divergent or convergent velocity signature at the surface or mid-levels, respectively, a descending radar reflectivity (Z) core (DRC), and environmental characteristics (e.g., downdraft convective available potential energy (DCAPE), steep lapse rates) that are favorable for downburst generation. However, divergence signatures only occur once downbursts have reached the surface and may not be observed at distances far from the radar, and prior studies have shown that not every downburst is reliably associated with mid-level convergence or a DRC. Similarly, environmental parameters are useful when forecasting for a broad area, but not every thunderstorm in an environment with conditions favorable for downbursts will produce one.

Recent work has begun exploring whether polarimetric radar offers insight into additional downburst precursor signatures. Previous studies using polarimetric radar to analyze downburst-producing thunderstorms have observed signatures such as a descending specific differential phase (K_{DP}) core and a trough of decreased differential reflectivity (Z_{DR}) collocated with decreased co-polar correlation coefficient (ρ_{hv}) extending below the melting layer. However, these studies either manually analyzed individual signatures or focused solely on case studies. This research expands on those studies by using the Multi-Cell Identification and Tracking (MCIT) algorithm to automate storm detection and analyze 41 downburst cases which span most regions of the contiguous United States. For each case, polarimetric radar variables, signatures,

and derived products hypothesized to potentially be relevant to downburst formation, including Z, K_{DP}, vertically integrated liquid (VIL), Z_{DR} column depth, convergence, and divergence, are analyzed to find any consistent patterns leading up to downburst events. Geographic and environmental variability are investigated as well.

Individual case analysis revealed that a DRC appeared within a volume scan of storm report (SR) time in 88% of cases, and a K_{DP} core was present and/or descending in 95% of cases, up to 15 to 30 minutes prior to the SR time in several cases. A Z_{DR} trough was present in 98% of cases with a collocated ρ_{hv} drop in 88% of cases within 10 minutes of the SR time for most cases, and the magnitude of low-level divergence and mid-level convergence reached a threshold of 0.0025 s^{-1} in 85% and 76% of cases, respectively. Analysis of all cases together revealed that divergence, velocity, and differential velocity display the most prominent signals near the surface at or just after the divergence signature (DS) time; aloft, K_{DP} at and 1 km below the freezing level, mid-level convergence, and VIL display the most prominent signals 5 minutes or more before the DS time. Analyses based on region and environmental favorability produced similar information, indicating that higher K_{DP} and lower divergence, velocity, VIL, and Z_{DR} column depth values were most common in eastern cases, as well as cases with WINDEX and 0–2-km LR less than 60 and 8 º km^{-1}, respectively. Conversely, higher divergence, velocity, VIL, and Z_{DR} column depth and lower K_{DP} values were more common in western cases, as well as cases with WINDEX and 0–2-km LR of greater than 60 and 8 º km^{-1}, respectively. These results aligned well with and confirmed findings from past studies.

Chapter 1

Introduction

1.1 What is a downburst?

Interest in researching downburst-producing thunderstorms began in the late 20th century after a well-documented aircraft crash at the John F. Kennedy International Airport in New York on 24 June 1975 killed 112 and injured 12 people. An investigation into the crash by the National Transportation Safety Board (NTSB; 1975) concluded that a sharp change in windspeed just short of the runway was the cause. Upon examining the meteorological conditions that lead to this event, Fujita and Byers (1976) coined the term "downburst" to describe these thunderstorms with an abnormally strong downdraft which produces an outburst of damaging winds at or near the surface. Since their discovery, much research has been conducted to understand and better predict downbursts in an effort to prevent future aircraft crashes, property damage, and threat to human and animal life.

An early finding of said research was the basic evolution of a downburst-producing thunderstorm. The first step involves the updraft of a storm suspending a core of rain, hail, and graupel aloft. Next, as shown in the vertical velocity tendency equation (Srivastava 1987)

$$\frac{\partial w}{\partial t} + w\frac{\partial w}{\partial z} = g\left[\frac{\Delta T_{ve}}{T_{ve}} - q_p - q_c\right], \tag{1}$$

where w is the vertical air velocity, g is the acceleration due to gravity, q_p is the precipitation mixing ratio, q_c is the cloud water mixing ratio, T_{ve} is the virtual temperature of the ambient

environment, and ΔT_{ve} is the virtual temperature difference between the ambient environment and the downburst core, there are two primary sources of negative buoyancy which promote downward acceleration within the storm: diabatic cooling and precipitation loading (Srivastava 1985, 1987; Hjelmfelt et al. 1989; Roberts and Wilson 1989). The diabatic cooling term in Equation 1 is represented as

$$g\left[\frac{\Delta T_{ve}}{T_{ve}}\right] \tag{2}$$

and arises from evaporating rain and sublimating and/or melting hail and graupel. The precipitation loading term in Equation 1 is represented as

$$g\left[-q_p - q_c\right] \tag{3}$$

and arises from excess water content aloft beginning to descend and dragging air within the storm downward. Non-hydrostatic pressure perturbations caused by storm rotation are a secondary source of negative buoyancy (Markowski and Richardson 2010) worth noting but are neglected in this study. It has also been found that the presence of ice particles in a storm produces more intense downdrafts due to the additional diabatic cooling from melting, and downdrafts are even more intense with larger environmental lapse rates, as descending parcels warm adiabatically and remain negatively buoyant so that less compensatory precipitation loading is needed; higher precipitation contents, due to increased precipitation loading and more diabatic cooling associated with melting or evaporation occurring; and higher concentrations of small precipitation particles, since smaller particles melt or evaporate more quickly than large ones (Srivastava 1987; Atlas et al. 2004). The final stage of downburst development occurs when the downdraft descends, reaches the ground, and winds, which can reach speeds equivalent to those associated with (E)F3 tornadoes (Wakimoto 1985), spread radially outward.

Fujita defined two types of downbursts based on the horizontal extent of the wind field (1981). The first is a “microburst”, which produces a divergent outflow with a diameter of less than 4 km across, and the second is a “macroburst”, which produces a divergent outflow with a diameter of more than 4 km across. Downbursts have also been categorized based on whether precipitation accompanies them as they reach the surface. A “dry” downburst is one in which precipitation evaporates completely before reaching the ground, creating virga below the cloud based as the downdraft continues to descend to the surface (Figure 1a), and a “wet” downburst is one in which precipitation reaches the ground and creates a distinct shaft from the cloud base to the surface (Figure 1b).

Figure 1. Examples of a) dry and b) wet downbursts (NWS). Photos by Brian Morganti.

1.2 Previous radar-based downburst studies

As mentioned in the section 1.1, downburst research became more common after a notable aircraft crash in 1975 caused by an abnormally strong downdraft in New York. Fujita and Caracena investigated this crash alongside two others (7 August 1975 in Denver, Colorado and 23 June 1976 in Philadelphia, Pennsylvania) and found that 5 to 50 minutes before the crashes, a “spearhead echo” in reflectivity formed north of the crash sites, moving faster than other nearby echoes (1977). Fujita also noted the radial wind damage patterns in forests caused by

downbursts, which were different from patterns caused by tornadic storms in that trees were flattened and spread outward from a central point (Fujita and Byers 1977).

Soon thereafter, several field projects were conducted in an effort to gather Doppler radar observations of these downburst events. Some of the more notable projects included:

- the Northern Illinois Meteorological Research On Downbursts (NIMROD) project in northern Illinois (Fujita 1978, 1985), which observed 50 microbursts in 42 days;
- the Joint Airport Weather Studies (JAWS) project near Denver, Colorado (McCarthy et al. 1982), which observed 186 microbursts, most of which were dry, in 86 days (Wakimoto 1985);
- the Classify, Locate, and Avoid Wind Shear (CLAWS) project near Chicago, Illinois (McCarthy and Wilson 1985);
- the FAA/Lincoln Laboratory Operational Weather Studies (FLOWS) project near the Memphis International Airport (Wolfson et al. 1985); and
- the Microburst and Severe Thunderstorm (MIST) project near Huntsville, Alabama (Dodge et al. 1986), which observed 62 microbursts in 61 days (Atkins and Wakimoto 1991).

Using the data from these projects and numerical weather models, researchers began trying to quantify and understand downburst environments, signatures, and precursors. It was found that the most favorable environments for downbursts to occur typically have high downdraft convective available potential energy (DCAPE; Emanuel 1994), large low-level temperature lapse rates (Srivastava 1985, 1987; Proctor 1989; Pryor 2015; Romanic et al. 2022), and a decreasing vertical distribution of moisture (Srivastava 1985; Proctor 1989). Using single-polarization variables, Wilson et al. (1984) defined a radar-measured differential velocity value of 10 m s^{-1} across the divergence center (from maximum inbound to maximum outbound

velocity within 4 km of each other) as the threshold for differentiating regular storms from downbursts, although the differential velocity across the divergence center in downbursts was typically much higher. Perhaps the most well-known downburst radar precursor signature is the descending reflectivity (Z) core (DRC), wherein the core of rain and hail being held aloft begins descending as its weight overcomes the strength of the updraft (Wakimoto and Bringi 1988; Roberts and Wilson 1989; Adachi et al. 2016; Kuster et al. 2016; Mahale et al. 2016). Horizontal convergence at mid-levels was also frequently observed prior to divergence at the surface due to mass continuity (Roberts and Wilson 1989; Heinselman et al. 2008; Vasiloff and Howard 2009). Some less frequently observed precursors included rotation below 3 km above ground level (AGL), a Z notch at mid-levels (about 5 to 7 km AGL) 2–6 minutes before the initial appearance of surface divergence, and a weakened Z gradient near the cloud top. Since these were observed less frequently, they were not considered reliable predictors of downbursts on their own, but increased the likelihood of intense downbursts alongside a DRC and mid-level convergence (Wakimoto and Bringi 1988; Roberts and Wilson 1989). During field projects, researchers were also able to photograph downbursts from less than 20 km away, superimpose research radar data onto it, and estimate its height based on the maximum Z center distance from the radar. They noted that the storms appeared to reach a maximum height about 8 minutes before outflow was observed at the surface (Wakimoto and Bringi 1988).

With the advent of polarimetric weather radars, even more downburst signatures and precursors have been investigated. One common polarimetric signature is a trough of decreased differential reflectivity (Z_{DR}) below the melting layer (Wakimoto and Bringi 1988; Roberts and Wilson 1989; Scharfenberg 2003; Richter et al. 2014; Pryor 2015; Kuster et al. 2016; Mahale et al. 2016) and an associated co-polar correlation coefficient (ρ_{hv}) drop (Dotzek and Friedrich

2009; Suzuki et al. 2010; Wang et al. 2018). This is caused by large ice particles (associated with lower values of Z_{DR} due to their often-spherical shape and/or tumbling as they fall) being forced below the melting layer by a strong downdraft. As they melt below the 0 ºC level, the particle types become more variable within the volume and any large wet hail may cause non-Rayleigh resonance scattering, so ρ_{hv} also decreases there. These both appear as the precipitation core within the downdraft is descending near the melting layer, prior to it reaching the surface, meaning they have potential use as precursors. Another frequently observed downburst signature is the presence of a specific differential phase (K_{DP}) core near the melting layer (Frugis 2018; Kuster et al. 2021), as well as its descent leading up to downburst occurrence. These are due to large quantities of melting ice particles, which results in an increase in negative buoyancy and hydrometeors subsequently being forced downward by a strong downdraft. Kuster et al. (2021) found that larger values and larger vertical gradients of K_{DP} near the melting layer were most often associated with more intense downbursts, and also pointed out that K_{DP} cores take longer than 15 minutes to evolve. Compared to the evolution of DRCs, which typically happen in less than 10 minutes, this allows for more observations within current operational volumetric update times of approximately 5 minutes.

However, there are caveats to using these signatures for downburst detection and prediction. Using DCAPE or environmental lapse rates to forecast downbursts is not always reliable since downdraft parcels mix with their environment and deviate from parcel theory. Dry air aloft may lower hydrometeor mass content, which decreases cooling (James and Markowski 2010) and lessens negative buoyancy. Most importantly, not every storm in an environment with these conditions produces a downburst. Mid-level convergence or surface divergence cannot be relied on alone to forecast downburst occurrence, as they are not observed in all cases (Isaminger

1988) and surface divergence does not appear until after the downdraft has reached the surface. Velocity signatures at the surface also become more difficult to observe as the storm's distance from the radar increases since the radar beam height begins to overshoot the low-levels. When using a DRC, the magnitude of descending reflectivity (Z) is uncorrelated with downburst intensity (Srivastava 1985; Pryor 2000) and Z alone does not indicate how much hail and/or rain is in a volume when both precipitation types are present (Carlin et al. 2016), meaning it may not be the best at quantifying storm cores. Lastly, previous studies investigating polarimetric radar signatures either manually analyzed individual signatures or, if they did investigate multiple signatures, focused solely on individual case studies, meaning many of these signatures or precursors may not be observed in every case.

1.3 Goals and objectives

This research expands on prior work by using the Multi-Cell Identification and Tracking (MCIT; Hu et al. 2019) algorithm to automate storm detection and analyze a large dataset of 41 wet downburst cases which span most of the contiguous United States. For each case, environmental conditions and single- and dual-polarization radar variables, signatures, and derived products hypothesized to potentially be relevant to downburst formation (e.g., Z, K_{DP}, vertically integrated liquid (VIL), Z_{DR} columns, and convergence/divergence) are analyzed with respect to downburst occurrence. By examining all these variables for each case of a large dataset, the objective is to find any consistent patterns leading up to downburst events and gather statistics on their frequency. Cases will also be examined by U.S. region to study the variability of the examined signatures in different geographic regions and identify any signatures or precursors specific to that area that can be used in operational forecasting. Ultimately, the goal of

this study is to identify which signatures or precursors, if any, improve the detection of and preparation time leading up to downburst occurrence, whether that be for aviation, special events such as concerts, sports, etc., or property and life in general.

Chapter 2

Data and Methods

There are three overarching steps necessary for this study: case selection, data acquisition, and qualitative and quantitative analysis. The goal of case selection is to choose downburst events that occur in weakly forced environments so that storm modes are less likely to be linear or supercellular and to ensure that the main forcing mechanisms within storms are localized diabatic cooling and precipitation loading. Several of the "traditional update" cases from Table 1 in Kuster et al. (2021) are used in this study because they met this goal, as well as the criteria discussed in section 2.1. However, storms in this study are not differentiated by strength. Next, the MCIT algorithm gathers the corresponding radar data for each case and automatically tracks all storms within a specified range of the input radar site. The downburst-producing storm is then isolated and extracted from the data to be qualitatively and quantitatively analyzed for signatures and/or precursors.

2.1 Case selection

Along with the aim of choosing cases in weakly forced environments, there are 3 other criteria used during the case selection step. The first is that the storm of interest, as well as the attendant official storm report, must exist between 30 and 100 km from the nearest Weather Surveillance Radar-1988 Doppler (WSR-88D) radar. These distances are calculated using the equation for radar beam height above radar level in a standard atmosphere (Rinehart 2010):

$$H = \sqrt{R^2 + \left(\frac{4}{3}r_e + H_0\right)^2 + 2R\left(\frac{4}{3}r_e + H_0\right)\sin(\varphi)} - \frac{4}{3}r_e \quad (4)$$

where H is the beam centerline height above sea level, H_0 is the radar height above sea level, R is the target distance from the radar, φ is the beam elevation angle in degrees, and r_e is the Earth's radius (6374 km). A distance of 30 km was determined to be the closest that a storm could be to a radar before the beam was unable to reach 10 km AGL (estimated for a radar elevation angle of 19.5º) so that radar variables such as Z_{DR} column depth and VIL would not be artificially decreased. Likewise, a distance of 100 km was determined to be the farthest that a storm could be from a radar before the beam was unable to scan down to 1.5 km AGL (estimated for a radar elevation angle of 0.5º), where divergence and low-level velocity signatures may occur.

The second criterion is that storms must occur in the latter half of 2013 or later, when the Next-Generation Radar (NEXRAD) network completed its dual-polarization upgrade. This is to ensure that polarimetric radar data is available for all cases. The final criterion is that all cases must have an official wind report from the National Centers for Environmental Information (NCEI) *Storm Data* database to get an estimated reference time for peak downburst intensity and storm report time, and get a sense of how much damage each downburst produced. An effort is also made to select cases from all regions of the U.S. to investigate any geographic variability in downburst radar characteristics and determine which, if any, are more prevalent in certain, or all, regions. However, downbursts are rare across the northern portions of the U.S. and west of the Rocky Mountains (Romanic et al. 2022). Furthermore, even if downbursts do occur near or west of the Rocky Mountains, they are rarely wet downbursts due to the higher elevation and typically dry air near the surface which evaporates precipitation. This is why most cases chosen for this study are east of the Rocky Mountains and farther to the south, which agrees with the

climatological distribution of downbursts (Romanic et al. 2022). In total, there are 41 downburst cases investigated across 26 days. These are split up by region, including the Northwest,

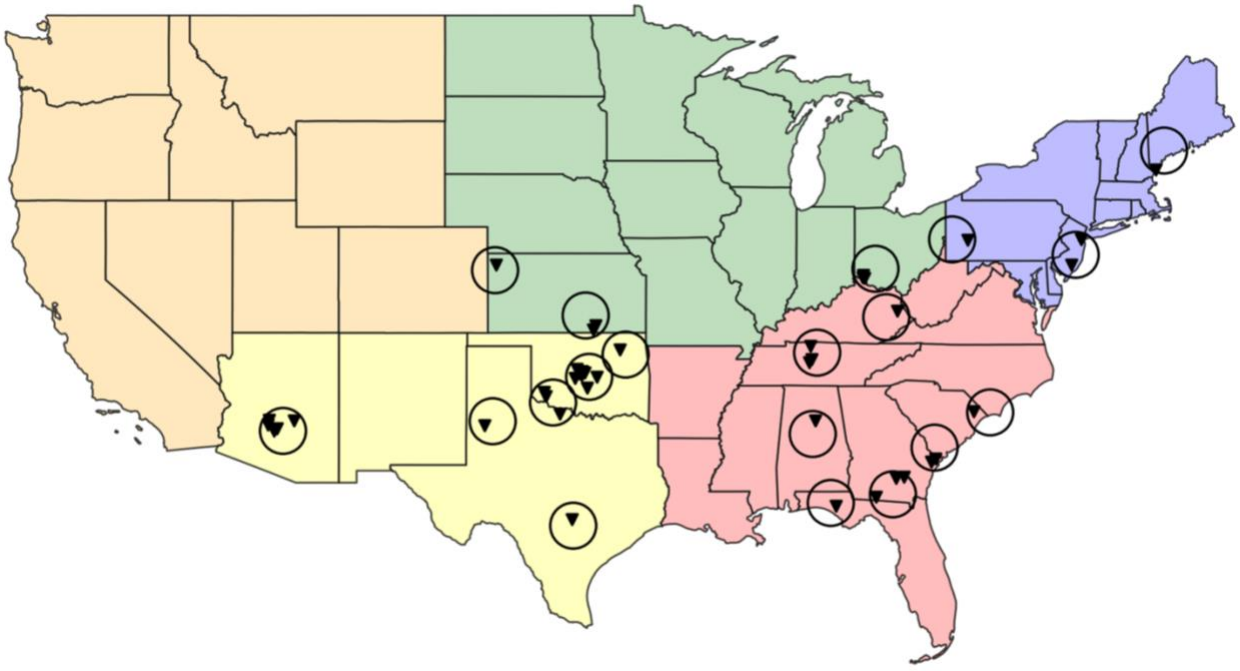

Figure 2. Map of the U.S. showing the Northwest (orange), Southwest (yellow), Midwest (green), Southeast (red), and Northeast (blue) regions with all 41 downburst case locations plotted (inverted triangles) and the WSR-88D radar locations and ranges (circles).

Southwest, Midwest, Southeast, and Northeast as shown by the 5 shaded regions in Figure 2. There are 4 cases in the Northeast, 6 cases in the Midwest, 19 cases in the Southwest, 12 cases in the Southeast, and ultimately no cases in the Northwest.

2.2 Storm identification and tracking using the MCIT algorithm

In this study, the MCIT algorithm is used to identify storms and track them through time by assigning them a global ID. The following description of how the algorithm functions summarizes the methods discussed in section 2.3 of Hu et al. (2019). First, NEXRAD WSR-88D Level 2 radar data for each case are downloaded from the Amazon Web Services NEXRAD repository containing the entire lifecycle of the reported downburst event to capture the full

evolution of the downburst-producing storm of interest. The radar data is pre-processed and interpolated onto a 1-km x 1-km Cartesian grid using an average of the nearest neighbor values weighted inversely by range. This field is then used to calculate the vertically integrated liquid (VIL; Greene and Clark 1972):

$$\text{VIL} = \sum 3.44 \times 10^{-6} \left[\frac{Z_i + Z_{i+1}}{2}\right]^{\frac{4}{7}} \Delta h \tag{5}$$

where VIL is in units of kg m^{-2}, Z is the radar reflectivity in mm^6 m^{-3}, Δh is the change in height (m), and $\frac{Z_i+Z_{i+1}}{2}$ is kept below 56 mm^6 m^{-3} to eliminate contributions from large ice-phase hydrometeors. Next, VIL is converted to units of dB by calculating $10\log_{10}(\text{VIL})$ so that identifying gradients and valleys in areas of lower VIL is not as difficult. This is then smoothed using a horizontal mean filter in a 3-by-3 grid point square.

Cell identification is completed next using the watershed algorithm described in Meyer (1994), which locates all local maximum VIL clusters in the domain, considered cell peaks, and assigns grid boxes (horizontal grid box size is 1 km x 1 km and vertical grid box size is 0.3 km) to them using watershed ridgelines in the calculated VIL field. Once any cell peaks reach a minimum of 50 grid boxes in size, they are assigned a local ID. Within the domain, each cell assigned a local ID is tested against surrounding cells to determine whether it has neighbors or not by searching within twice the radius of the cell's longest dimension. If a cell with an assigned local ID other than that of the cell of interest or the cell being compared against exists between the peaks of each cell, then they are not considered neighbors, and vice versa. After all of the neighboring cells are identified, they are tested to see if they should be merged together or not using the valley depth, or saddle point, between them. When VIL values between neighboring

cells fall below 2 dB or less, then the cell with a lower VIL maximum is merged with the stronger cell and assigned the same local ID.

The horizontal VIL maps from the first stage and the map of local IDs from the second stage are used as input for the final stage: cell tracking. The MCIT algorithm does this by comparing consecutive VIL maps and checking for overlapping cells. Between one map at time n and the following map at time n+1, a shifting vector based on the distance between sequential cell peaks is created and updated for each cell. Next, using the same logic as in Table 3 of Rosenfeld (1987), except with VIL instead of reflectivity and common rain volume, the algorithm determines whether cells in the map at time n+1 are continuations of cells in the map at time n or not. To be considered a continuation, cells must meet the following criteria: the integrated common VIL of both cells must be 50% or more of the total VIL in the smallest cell, and VIL peaks of each cell must be inside the common area of both cells. If a case arises where the latter condition is not met, then the integrated common VIL must be 75% or more of the total VIL in the smallest cell, and if this condition is also not met, then the cell at time n is considered a merger or split as long as the integrated common VIL is 25% or more of the total VIL in the smallest cell. If a cell at time n has 2 or more continuation cells at time n+1, the cell with the largest integrated common VIL is used as the continuation cell and the rest are considered splits; if a cell at time n+1 has 2 or more continuation cells at time n, then they are merged. Once this is complete for all cells in the domain, they are assigned a global ID (hereafter referred to as a storm ID (SID)) throughout their lifetime which is used to distinguish the downburst-producing cell of interest from all other cells in this study.

The final step in identifying and tracking the cells involves using the Python Atmospheric Radiation Measurement (ARM) Radar Toolkit (Py-ART; Helmus and Collis 2016). Upon

plotting the SIDs of all cells at each volume scan along with a marker at the location of the storm report, the SID of the downburst-producing cell for each case is found by determining which cell is over the storm report location marker at the storm report time and tracking it throughout its

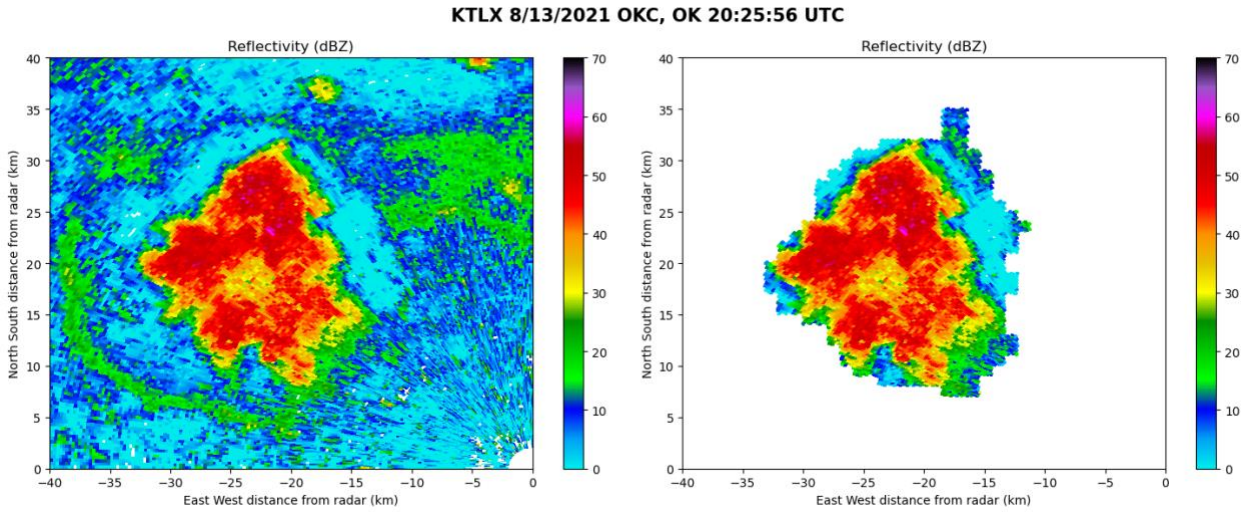

Figure 3. Example of the MCIT SID being used to isolate an individual convective core from surrounding noise, clutter, or other cells using Py-ART. From KTLX on 13 August 2013.

lifecycle. In 13 of the 41 cases, cells merged at some point in their lifetime, causing the SID to change as it took on the SID of the cell with the larger maximum VIL. To make tracking these cases for analysis easier, a new common SID is manually assigned to the cell of interest leading up to and after the cells merged. After all cases have a single, unique SID, they can be filtered so that only the downburst-producing cell of interest is analyzed, as shown in Figure 3.

2.3 Choosing and calculating radar variables of interest

Prior to quantitative and qualitative analysis, variables and features believed to be relevant to the formation and occurrence of downbursts are chosen. Environmental variables that are chosen include the 0–2-km temperature lapse rate (LR) and the Wind Index (WINDEX; McCann 1994); raw radar variables chosen include Z, velocity, Z_{DR}, and ρ_{hv}; calculated radar variables chosen include K_{DP}, VIL, divergence, and convergence; and features chosen include

Z_{DR} column depth, DRC, K_{DP} cores, and descending K_{DP} cores. For each case, the vertical distribution of each variable is extracted at every radar gate within the storm cell of interested and interpolated to a common height grid of 50 m for comparing across different heights. Calculation methods and explanations of all calculated variables or features are discussed in the next several subsections, and once all values of all necessary variables are obtained, they are stored in a Py-ART radar object and saved to a Network Common Data Form (NetCDF4) file.

2.3.1 Environmental variables

The two environmental variables investigated herein are the 0–2-km LR and WINDEX value at the nearest radar to the downburst event location. The 0–2-km LR is chosen because steeper low-level lapse rates are more favorable for downbursts (Romanic et al. 2022; Srivastava 1987). As the LR approaches dry adiabatic (9.8 ºC km^{-1}), downdrafts at that level will become more negatively buoyant and, presumably, more intense as they reach the surface. Similarly, WINDEX is chosen because it incorporates the surface to freezing level LR and mixing ratios. As WINDEX values increase, potential downburst intensity is expected to increase as well.

The variables necessary to calculate LR and WINDEX such as temperature, relative humidity, and isobaric geopotential height are gathered using hourly data from the Rapid Refresh (RAP; Benjamin et al. 2016) analysis via the NCEI Thematic Real-time Environmental Distributed Data Services (THREDDS) data server. Profiles of each variable at the hour preceding the downburst storm report time and at the location of the radar site for each case are recorded and used to calculate other necessary variables such as mixing ratio, and then used to calculate LR and WINDEX. For the 0–2-km LR, the mean lapse rate over the lowest 2 km AGL is taken. For WINDEX, Equation 6 from McCann (1994) is used:

$$\text{WINDEX} = 5[H_M R_Q(\Gamma^2 - 30 + Q_L - 2Q_M)]^{0.5} \quad (6)$$

where H_M is the freezing level height AGL (km), Γ is the temperature lapse rate from the surface to the freezing level (ºC km^{-1}), Q_L is the mixing ratio of the surface to 1 km AGL layer (g kg^{-1}), $R_Q = {Q_L}/{12}$ and is capped at a maximum of 1 g kg^{-1}, and Q_M is the mixing ratio at the freezing level (g kg^{-1}). The height of the freezing level and the -20 ºC level are also recorded for analysis of Z_{DR} troughs, ρ_{hv} drops, Z_{DR} column depth, and Z, discussed in the following sections.

2.3.2 K_{DP} and K_{DP}-related variables

Considering the results from Kuster et al. (2021), K_{DP} is chosen to be investigated because it shows potential as a downburst precursor, and possibly a downburst intensity indicator. It is calculated for all cases with the so-called Vulpiani method (Vulpiani et al. 2012) using the Py-ART function (Helmus and Collis 2016) with pre-filtering applied to the raw differential phase shift data and a window size of 8. From this calculation, a novel volume-integrated value of K_{DP} is also computed within ±500 m of the freezing level and 1-km beneath it, using a threshold of 1 º km^{-1} or greater to isolate the K_{DP} core. This is done by first calculating gate area on each tilt according to the equation for the area of a sector, $rdrd\theta$ where r is the slant range and θ is the azimuth, then multiplying each gate area by 50 m, the height of each vertical bin. The sum of the resulting gate volumes multiplied by the K_{DP} values is then calculated and divided by the storm volume in that layer. This value is then multiplied by 1×10^{-9} to get units of º km^{-1}, as shown in Equation 7:

$$\frac{\sum(x_i * y_i)}{\sum y_i} * 1 \times 10^{-9} \quad (7)$$

where x_i represents K_{DP} and y_i represents the interpolated gate volume.

2.3.3 Low-level divergence and mid-level convergence

Low-level divergence and mid-level convergence are chosen to be investigated because they are common signatures associated with downburst occurrence. They are computed using velocity data at the lowest radar beam tilt (0.5º) and between 3 to 7 km AGL, respectively. To start, a median filter with a kernel size of 5 is applied to the velocity data in an effort to decrease noisiness and the occurrence of outlier values. Then, the radial divergence is calculated by taking the gradient of the median-filtered radial velocity over a sliding 4-km window in the radial direction. All resultant positive values denote divergence, and all resultant negative values denote convergence. To analyze low-level divergence, positive values at the lowest tilt (0.5º) are investigated, and to analyze mid-level convergence, negative values within 3 to 7 km AGL are investigated.

A novel area-integrated divergence is also computed for this study which uses the same gate area calculation as for volume-integrated K_{DP} multiplied by the low-level divergence values, which are summed and multiplied by 1×10^{-6} to get units of s^{-1}, as shown in Equation 8, where

$$\sum (x_i * y_i) * 1 \times 10^{-6} \tag{8}$$

x_i represents gate area and y_i represents divergence. Area-integrated calculations are done for low-level divergence to investigate how the low-level divergence signature grows as the downburst spreads horizontally.

2.3.4 Low-level velocity and differential velocity

Similar to divergence and convergence, low-level velocity and differential velocity are chosen to be investigated because increased maxima of both are common signatures associated with downburst occurrence. The 0.5° velocity data is used for both variables, and a median filter

is again applied to reduce noisiness and outlier values. From this data, the maximum velocity and differential velocity are computed within 5 km of the downburst-producing-cell's maximum VIL to estimate outflow strength and compare to the divergence. To get the maximum velocity of each radar scan, the maximum absolute value of inbound and outbound velocities is calculated and used. To get the maximum differential velocity of each radar scan, the minimum measured value is subtracted from the maximum measured value of the inbound and outbound velocities.

2.3.5 Maximum VIL, Z_{DR} column depth, and Z at -20 ºC

Maximum VIL is chosen to be investigated because larger values within a downburst-producing cell may be indicative of precipitation loading, a source of negative buoyancy and precursor to downburst occurrence. Using VIL data, maximum values are found and recorded within the cell of interest. Similarly, Z at -20 ºC is chosen to be investigated because it may indicate robust ice particle growth and a strong updraft, and if an increase then decrease in Z occurs here prior to downburst occurrence, it could be indicative of a DRC (Wakimoto and Bringi 1988; Roberts and Wilson 1989; Adachi et al. 2016; Kuster et al. 2016; Mahale et al. 2016). This variable is obtained by finding Z values at the -20 ºC isotherm height over the cell's lifetime.

Finally, Z_{DR} column depth is considered. As defined by Snyder et al. (2015), a Z_{DR} column is an upward extension of Z_{DR} values 1 dB or greater above the freezing level. These are a result of liquid and mixed-phase particles, which typically have higher Z_{DR} values owing to their horizontally oriented shapes, being lofted in a storm's updraft above the freezing level. The Z_{DR} column depth is chosen to be investigated because the presence of one can be indicative of growing convection, and a deeper Z_{DR} column may indicate a stronger updraft (Snyder et al.

2015). This variable is computed using the same method as Snyder et al. (2015) wherein a 5-range-gate moving average filter is applied to the Z_{DR} data to reduce noisiness, then the filtered data is placed onto a 3D grid with a 0.0025° × 0.0025° grid spacing in latitude and longitude and a 250 m grid spacing in height. Freezing level is provided from the RAP, and the number of vertical grid points with Z_{DR} values 1 dB or greater are counted at each horizontal grid point to estimate the depth of the Z_{DR} column above the freezing level. A Gaussian filter is then applied to this output to smooth the resulting data.

2.4 Case analysis

2.4.1 Time–height plots

Once all radar variables of interest are calculated for each case, time–height plots are created of all raw radar variables, K_{DP}, divergence, and convergence to investigate the presence of downburst signatures and/or precursors. Doing so collapses the radar data from four dimensions (time and space) into a two-dimensional, Lagrangian, time–height plot to help elucidate the evolution of radar signatures within the downburst-producing storm. The extracted columns of each variable are placed into height bins that span every 500 m up to 3 km, every 1 km up to 8 km, then every 2 km up to 16 km to due to worsening vertical resolution with height owing to data gaps between elevation angles. Afterwards, percentiles of some variables at each height bin are calculated as a way to discard any outlier values and isolate the most intense part of the storm (i.e., the core). For Z and K_{DP} in this study, the 95th percentile value is used for analysis. Both 90th and 99th percentile are tested as well, but they provide similar qualitative information. For Z_{DR}, the 50th percentile above the 95th percentile Z is used to gauge whether values near the storm core are generally higher and indicative of rain, or closer to 0 dB and

therefore more likely indicative of hail. The 10th percentile of ρ_{hv} above 95th percentile Z is used to focus on areas near the storm core with lower values, where mixed-phase precipitation is most likely. Lastly, 90th percentile divergence and 10th percentile convergence are used to isolate the more extreme values within and underneath the downburst-producing storm.

To determine if DRCs and/or K_{DP} cores at the freezing level and descending K_{DP} cores are present, the time–height plot of 95th percentile K_{DP} is plotted with 95th percentile Z contours (intervals of 50, 55, and 60 dBZ). For DRCs, if contours of 55 dBZ or greater are generally descending leading up to the storm report time, a DRC is considered present. For K_{DP}, if concentrated values of 1 ° km^{-1} or more are near the freezing level, a K_{DP} core is considered present, and if that core is descending leading up to the storm report time, a descending K_{DP} core is considered present. Z_{DR} troughs and collocated ρ_{hv} drops are determined in a similar way by plotting the median Z_{DR} and 10th percentile ρ_{hv} at 95th percentile Z side-by-side. If values of Z_{DR} approaching 0 dB reach a minimum below the freezing level leading up to the storm report time, then that case is considered to have a Z_{DR} trough. If values of ρ_{hv} approaching 0.96 appear in the same location as the Z_{DR} trough, then that case is considered to have a collocated ρ_{hv} drop. Lastly, 90th percentile convergence and divergence are plotted to determine if a low-level divergence or mid-level convergence signature appears. Values close to 0.0025 s^{-1} or more that appear at or after the storm report time in the lowest 3 km are considered low-level divergence signatures, and convergence values near 0.0025 s^{-1} or more that appear within 3 to 7 km leading up to the storm report time are considered mid-level convergence signatures.

2.4.2 Time series plots

All raw and calculated radar variables and Z_{DR} column depth are then plotted relative to the storm report, divergence signature, or maximum VIL time. The initial storm report times are provided by the NCEI *Storm Data* database, maximum VIL times are found objectively, and the divergence signature time is found by plotting the velocity and divergence of each radar PPI scan and using the time of the scan that a divergence signature first appears, presumably when the downdraft reaches the surface. For each variable, the values are interpolated from -45 to +45 minutes relative to the anchor time and all cases are composited and plotted together. To better visualize trends in the values and reduce the influence of outliers, the median, 25th percentile, and 75th percentiles are also plotted for each variable. These again are subjectively analyzed, and signatures or precursors are determined to be present based on when they appear and how strong of a signal they display. Similar plots but with values of each variable normalized by each time series' maximum value are created as well to see if and when signatures appear relative to the anchor time, regardless of storm size or magnitude of the respective signatures.

Plots of median, 25th percentile, and 75th percentile values relative to the divergence signature time are also made for cases divided by U.S. region (east versus west), WINDEX value (greater or less than 60), and 0–2-km LR (greater than or less than 8 ºC km^{-1}). These are used to determine whether geographic location of or environmental conditions near a downburst event impact the presence of signatures or precursors observed in plots with all cases.

2.4.3 Occurrence statistics

The final step of analysis involves plotting cumulative frequency distribution (CFD) plots of quantitative variables (Z, K_{DP}, divergence, convergence, velocity, differential velocity, Z_{DR}

column depth, and VIL) to show the entire distribution of the typical ranges for all of these variables. CFD plots are also made for each region shown in Figure 2, and those values are compared to the values calculated using all cases to see if any relative geographic variability exists. Thresholds of each variable considered to differentiate "stronger" storms from "weaker" ones are used as well to determine the percentage of cases that meet them. This includes 1 º km^{-1} for K_{DP} (Kuster et al. 2021), 0.0025 s^{-1} for divergence and convergence (Dance and Potts 2002; Wilson et al. 1984), 25 m s^{-1} for maximum velocity (Smith et al. 2004), 40 m s^{-1} for differential velocity (Smith et al. 2004), 3 km for Z_{DR} column depth (Snyder et al. 2015), 30 kg m^{-2} for VIL (Kitzmiller et al. 1995), 50 dBZ for Z at -20 ºC, 8 º km^{-1} for 0 to 2 km LR (Srivastava 1985, 1987), and 60 for WINDEX (McCann 1994). Thresholds for Z_{DR} column depth, VIL, and WINDEX are the average values across cases found in each study rounded to the nearest integer, and the threshold for Z at -20 ºC is chosen subjectively.

Chapter 3

Results and Discussion

3.1 Time–height plots of individual cases

Time–height plots of each case relative to the time of the first storm report (SR) are first examined to manually identify descending cores of Z and K_{DP}, Z_{DR} troughs and ρ_{hv} drops within storm cores, and low-level divergence signatures (DS) and mid-level (i.e., 3 to 7 km AGL) convergence signatures. The time of the first SR associated with a downburst event is marked by a vertical line on each plot to examine the occurrence of each of these signatures with respect to the SR time, and the freezing level is marked by a horizontal line on each plot to estimate where precipitation is beginning to melt.

In order to determine whether any downburst signature is present for each case, all variables are examined from 45 minutes before until 45 minutes after the SR time. However, the window used to consider a given signature present and associated with the downburst event is 30 minutes leading up to, and 10 minutes following, the SR time. This window is expected to allow storms enough time to grow and collapse, but prevent any signatures not associated with the SR from being analyzed, given some cases involve cycling storm cells. The 10 minutes following the SR time are also considered due to the uncertainty associated with accurate SR times for each case. The first signatures investigated are the descending Z and K_{DP} cores using local maxima of 95th percentile K_{DP} with contoured 95th percentile Z. An example of a case where both descending Z and K_{DP} cores are present is seen in Figure 4 from KEWX on 27 June 2022. A Z

core with values over 60 dBZ descends from about 6 to 3 km AGL starting at 18:43 UTC over roughly 8 minutes and a K_{DP} core with values over 3 ° km^{-1} descends from about 3 to 2 km AGL starting at 18:48 UTC over roughly 5 minutes. Overall, 36 out of 41 cases contained an

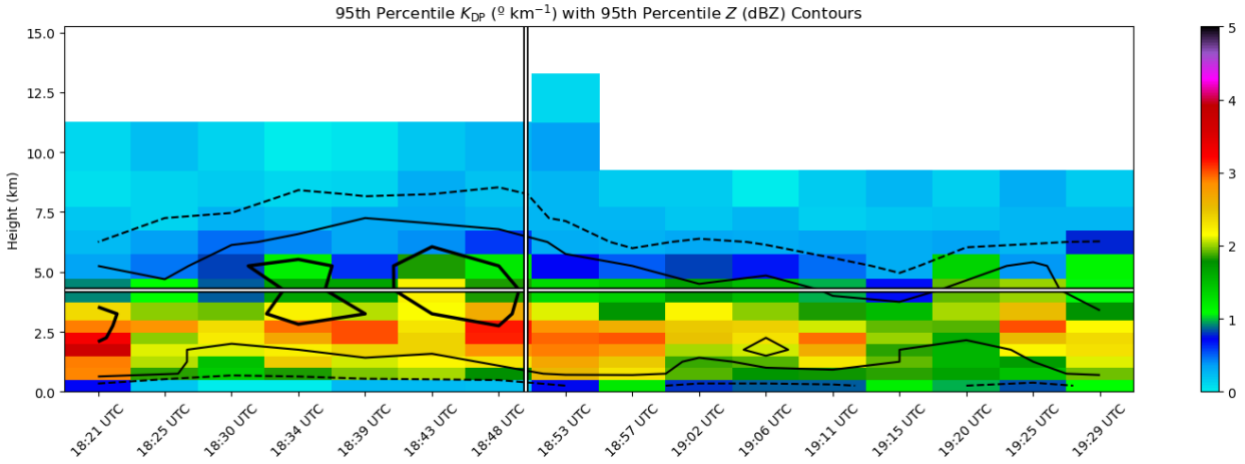

Figure 4. Time–height plot of 95th percentile K_{DP} (shading) and Z (black contours, dashed line is 50 dBZ, thin solid line is 55 dBZ, and bold solid line is 60 dBZ) from KEWX on 27 June 2022. The vertical line marks the storm report time, and the horizontal line marks the estimated freezing level.

identifiable descending Z core and 39 out of 41 cases contained an identifiable descending K_{DP} core. It is worth noting that nearly all descending Z cores are present within one volume scan of the SR time, and almost a quarter of the descending K_{DP} cores appear 15 to 30 minutes prior to the SR time which aligns well with the work of Kuster et al. (2021), who also found that K_{DP} cores evolve more slowly than Z cores, and they often reach a maximum 14 minutes prior to peak downburst intensity. The rest of the K_{DP} cores appear within a scan of the SR time, similar to the Z cores.

Z_{DR} troughs and collocated ρ_{hv} drops are analyzed in a similar way by looking at time–height plots of median Z_{DR} and 10th percentile ρ_{hv} at and above the 95th percentile Z for each case. The appearance of these signatures is hypothesized to be associated with medium to large hail falling below the environmental freezing level within the storm's downdraft. A case is said to have a Z_{DR} trough if Z_{DR} values less than approximately 1 dB extend below the plotted freezing

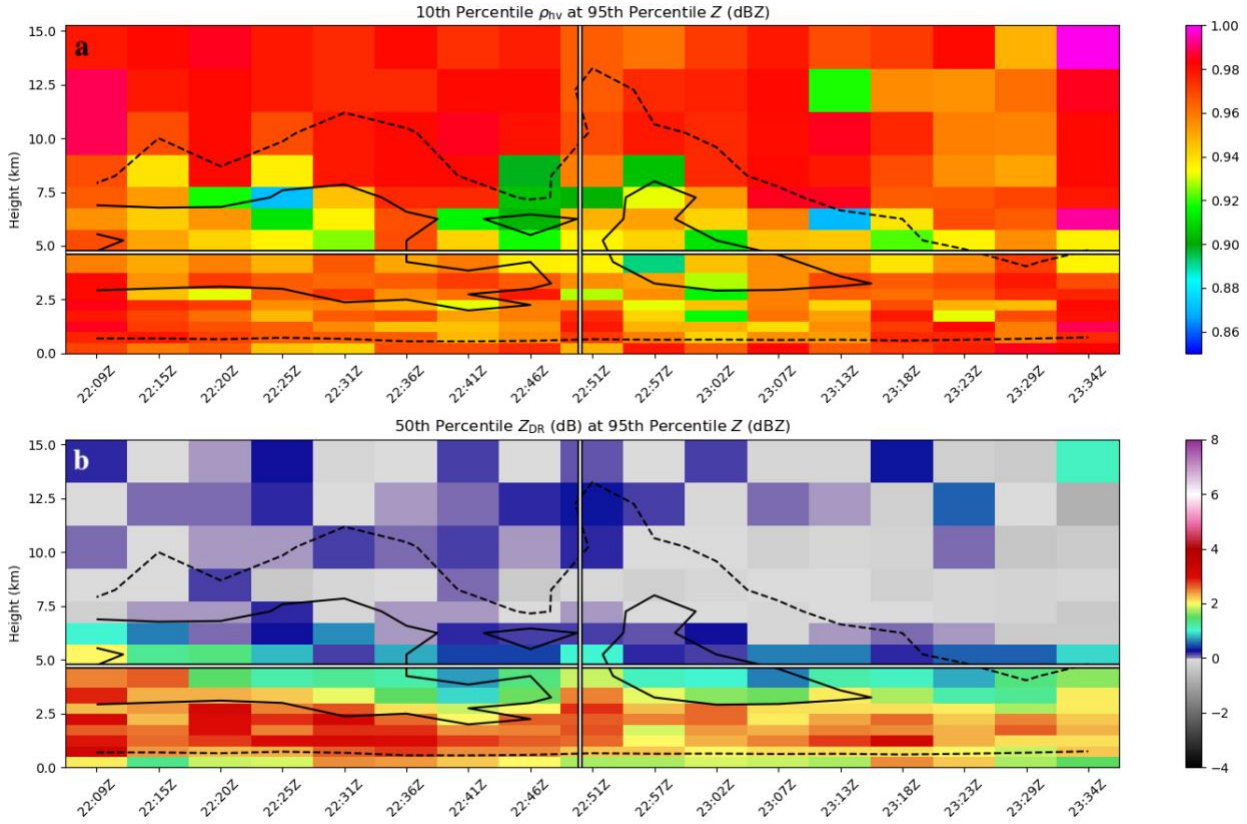

Figure 5. Time–height plot of a) 10th percentile ρ_{hv} at the 95th percentile Z (shaded) with 95th percentile Z contours as in Figure 4 and b) median Z_{DR} at the 95th percentile Z (shaded) with the same 95th percentile Z contours from KCLX on 22 June 2015. The vertical line marks the storm report time, and the horizontal line marks the estimated freezing level.

level within the time window. Similarly, a case is said to have a collocated ρ_{hv} drop if ρ_{hv} values less than approximately 0.96 extend below the plotted freezing level within 1 volume scan of the Z_{DR} trough appearance. These threshold values are chosen arbitrarily but are believed to differentiate volumes with purely water hydrometeors (i.e., Z_{DR} values of 1 dB or greater and ρ_{hv} values closer to 1.00) from those with mixed hydrometeors (i.e., closer to 0 dB and reduced ρ_{hv} values). An example of a case where both signatures are present is shown in Figure 5 from KCLX on 22 June 2015. A Z_{DR} trough begins forming at 22:25 UTC (Figure 5b), 25 minutes before the SR time, with ρ_{hv} values of 0.95 (Figure 5a) and below appearing in the same volume scan near the freezing level. In the next 5 volume scans, the depressed Z_{DR} values extend farther below the freezing level, reaching a minimum height of roughly 4 km at 22:41 UTC.

Immediately following this, ρ_{hv} values near the freezing level also drop to about 0.90. It is worth noting that the Z contours of this plot show a descending Z core of 60 dBZ or greater collocated with the Z_{DR} trough and ρ_{hv} drop, indicating a descending precipitation core likely containing large melting hail. Overall, 40 out of 41 cases show a Z_{DR} trough and 36 out of 41 cases show a ρ_{hv} drop collocated with a Z_{DR} trough. Although these signatures appear within 10 minutes of the SR time for a majority of cases, they appear more than 10 minutes before the SR time in 8 cases, more than 20 minutes before in 5 cases, and up to 30 minutes before in 3 cases.

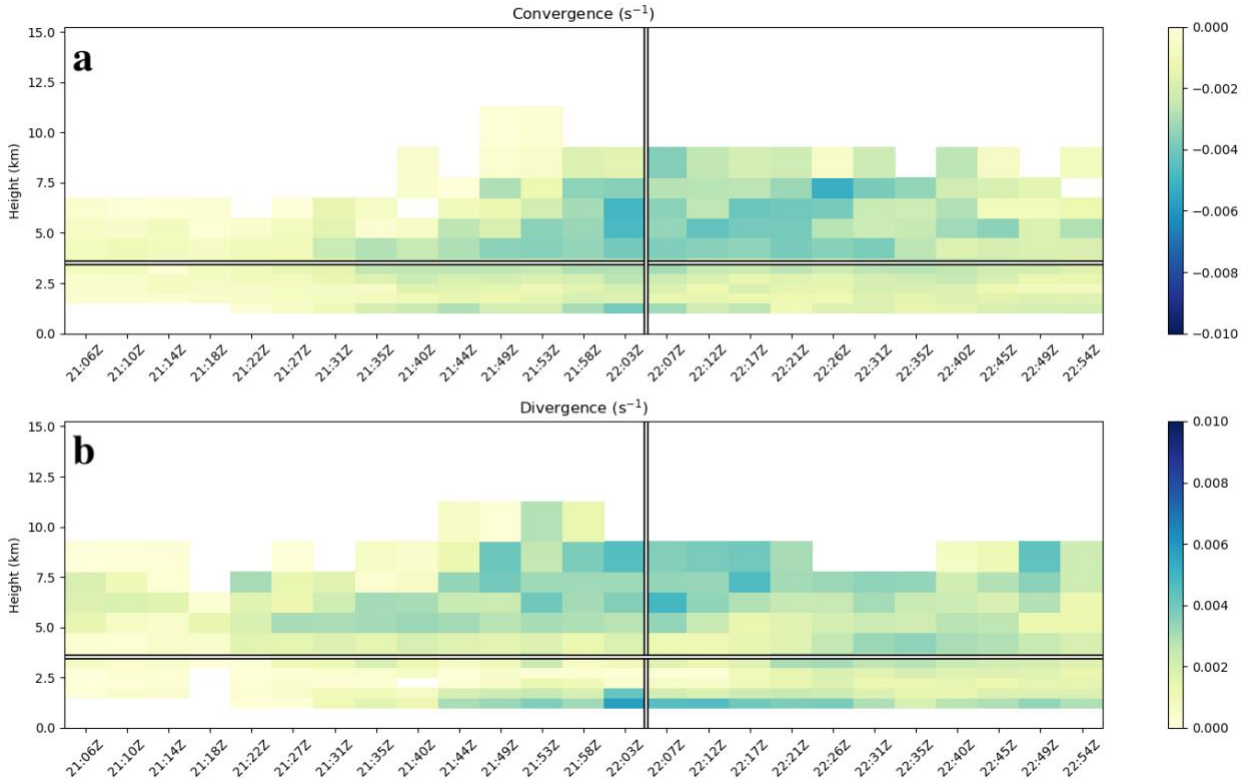

Figure 6. Time–height plot showing the a) 90th percentile convergence and b) 90th percentile divergence from KGLD on 30 July 2013. The vertical line marks the storm report time, and the horizontal line marks the estimated freezing level.

After investigating Z_{DR} troughs as a downburst precursor signature, Z_{DR} columns are also explored. Maximum Z_{DR} column depths above the freezing level are found for each case; because this is a scalar variable, time–height plots are not created. In general, all storms contain a Z_{DR} column that extends at least 1.8 km or more above the freezing level. More specifically, 21

out of 41 cases produce a Z_{DR} column that reaches over 3 km above the freezing level, 13 out of 41 cases produce a Z_{DR} column that reaches over 4 km above freezing level, and 2 out of 41 cases produce a Z_{DR} column that reaches over 5 km above freezing level. This variable also proves useful as a potential precursor given that 37 out of 41 cases reach a maximum Z_{DR} column depth above freezing level 5 or more minutes prior to SR time. Notably, 15 out of these 37 cases maximize in the 5 minutes preceding SR time, 17 other cases maximize between 5 and 15 minutes prior to SR time, and the remaining 5 cases maximize between 15 and 25 minutes prior to the SR time.

The final two signatures explored using time–height plots are low-level divergence and mid-level convergence. Time–height plots of the 90th percentile of divergence data greater than 0 s^{-1} and the 10th percentile of divergence data less than 0 s^{-1} (i.e., 90th percentile of convergence) are plotted. Using the same time window as before, an event is said to have low-level divergence or mid-level convergence if values of each reach 0.0025 s^{-1} or greater, respectively (Dance and Potts 2002; Wilson et al. 1984). Different thresholds were also explored based on other studies (Fujita and Byers 1976; Knupp 1989; Smith et al. 2004) with qualitatively similar results. Figure 6 (from KGLD on 30 July 2013) displays a case where mid-level convergence maximizes near 6 km AGL in the scan prior to the SR time (Figure 6a), and where low-level divergence maximizes at the same time in the lowest 1 km AGL (Figure 6b).

Overall, 35 out of 41 cases showed mid-level convergence and 31 out of 41 cases showed low-level DS. Given the operational use of these two signatures when identifying downbursts, these frequencies are lower than anticipated. This may be due to an overly stringent threshold of 0.0025 s^{-1} but is also likely caused by poorer resolution of storms farther away from their closest radar. In cases where storms are farther away, radar beam broadening lowers the resolution of the

data at all heights, potentially underestimating the data values (Smith et al. 2004), and the beam has potential of overshooting the low-levels, where divergence maxima would occur.

3.2 Analysis of all cases

3.2.1 Storm-report-relative plots

Following the individual case analysis, plots including all 41 cases are also made for radar variables of interest in an effort to identify consistent time series signatures relative to SR time. These variables include the maximum divergence, area-integrated divergence, 95th percentile K_{DP} at and 1-km below the freezing level, volume-integrated K_{DP} at and 1 km below the freezing level, maximum velocity and differential velocity at the lowest elevation angle, maximum mid-level convergence, maximum VIL, maximum Z_{DR} column depth, and 95th percentile Z at -20ºC.

Time series of each variable for every case centered on the SR time are interpolated and plotted from 45 minutes prior to 45 minutes after the SR time, which is labeled at t = 0 minutes. However, this method frequently results in a lack of a discernable signal, with a considerable number of cases included and many overlapping lines. Another issue that arises when using this method is when cases have outliers. For example, in the case of maximum differential velocity, there is a large cluster of cases centered around 20 m s^{-1} for most of the time window, however, there are also several cases with outliers that reach up to 60 m s^{-1} and they all occur at different times. In an effort to mitigate this and make interpretation easier, the median, 25th percentile, and 75th percentile across all cases is calculated and plotted for each volume scan.

Analysis of the SR-relative plots of all 12 variables reveals that most of them do display a trend over time, but they are not very prominent. The first several time series examined in Figure 7 are the four K_{DP} related variables. Starting with 95th percentile K_{DP} at the freezing level (Figure

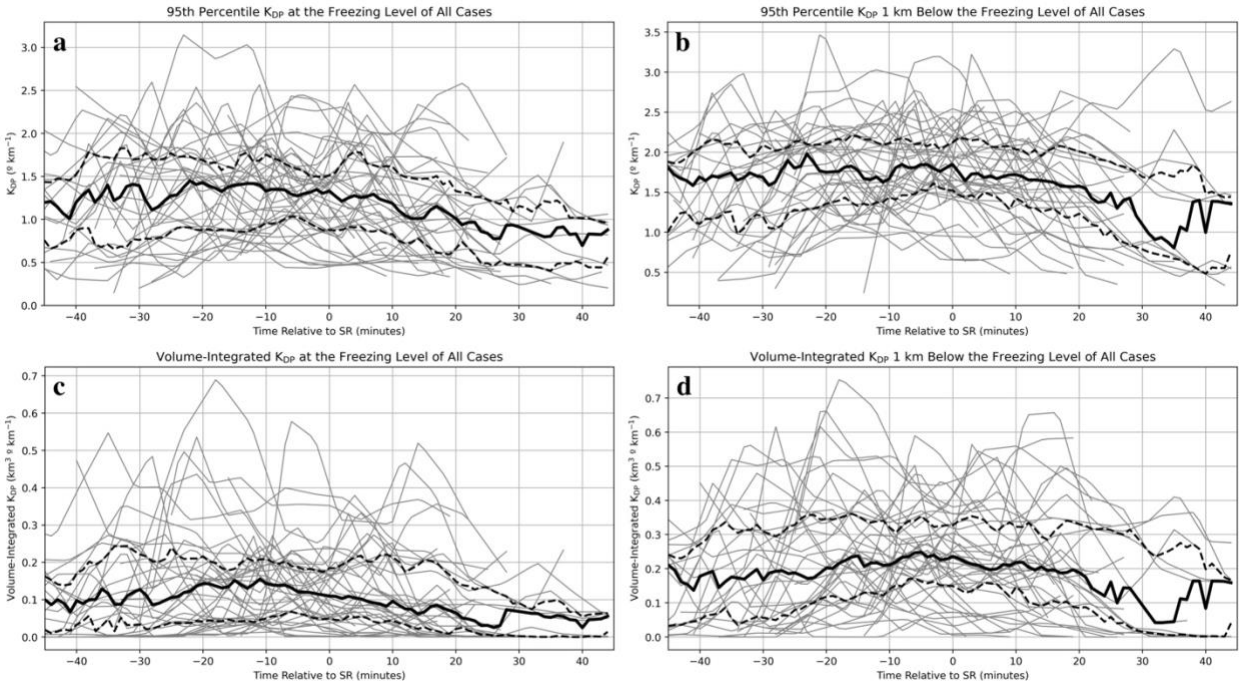

Figure 7. SR-relative time series of a) 95th percentile K_{DP} at the freezing level (° km^{-1}), b) same as a, but at 1-km below the freezing level (° km^{-1}), c) volume-integrated K_{DP} at the freezing level (° km^{-1}), and d) same as c, but at 1-km below the freezing level (° km^{-1}). The gray lines represent values of each case, the black dashed lines represent the 25th and 75th percentile values of all cases, and the solid black line represents the median value of all cases.

7a), the median is rather stagnant at just under 1.5 ° km^{-1} through the SR time, then it slowly decreases for the remaining time. The same variable at 1-km below the freezing level (Figure 7b) has a similar pattern, remaining stagnant at just under 2 ° km^{-1}, but it does not decrease as much after the SR time. Volume-integrated K_{DP} at the freezing level (Figure 7c) has a slight signal where it peaks near 10 minutes before the SR time, and the same variable at 1-km below the freezing level (Figure 7d) slightly increases until near 5 minutes before the SR time. In all of these plots, there are several outliers and peaks which occur at all times relative to the SR time, so it is unsurprising that there is no obvious signal in the median time series. It is worth noting that values 1-km below the freezing level are larger than those at the freezing level for both variables, likely because more melting has occurred, and more liquid hydrometeors are present at that level.

Figure 8 displays the composited time series of maximum divergence, area-integrated divergence, maximum velocity, and maximum differential velocity at the lowest beam tilt.

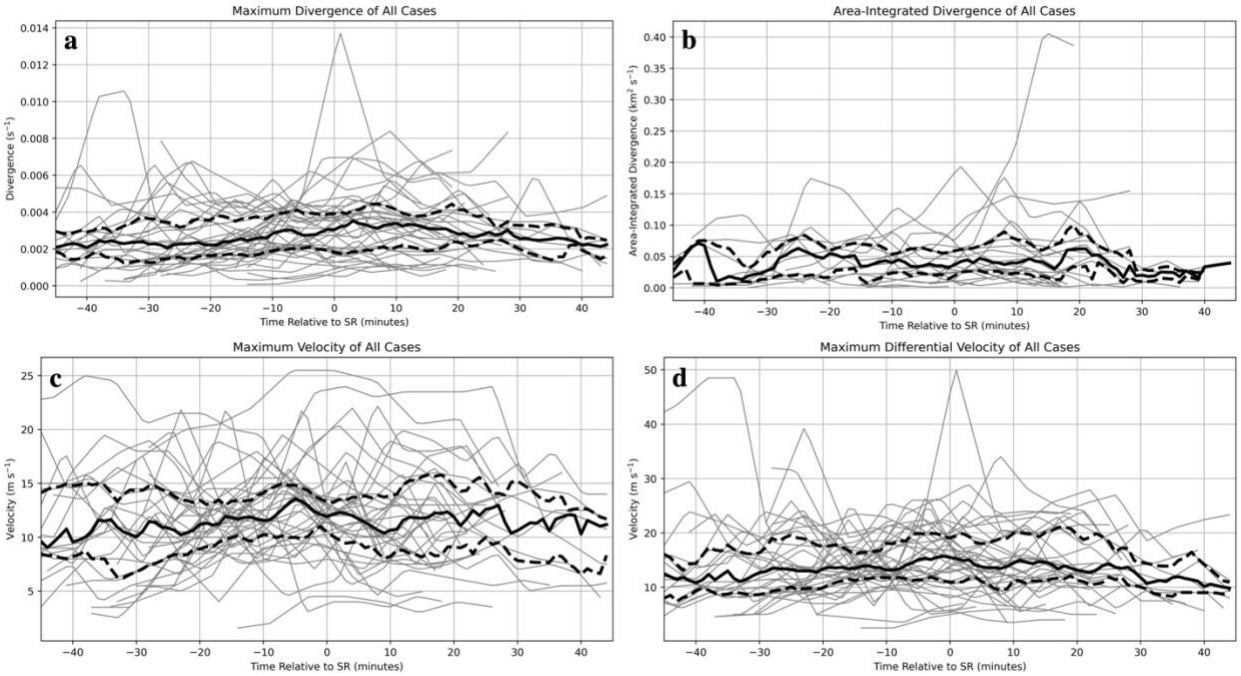

Figure 8. Same as Figure 7, except of a) maximum divergence (s^{-1}), b) area-integrated divergence (s^{-1}), c) maximum velocity (m s^{-1}), and d) maximum differential velocity (m s^{-1}) of all cases.

Median maximum divergence (Figure 8a) peaks near 5 minutes after the SR time at just under 0.004 s^{-1}, as expected since the outflow winds become more intense after reaching the surface. For area-integrated divergence (Figure 8b), there is no clear signal, and the median remains nearly stagnant at just under 0.05 s^{-1}. Median maximum velocity (Figure 8c) has a more prominent peak of about 14 m s^{-1} near 5 minutes before the SR time, and median maximum differential velocity (Figure 8d) has a slight, gradual increase up to the SR time then decreases, and also remains below 15 m s^{-1}.

The last 4 SR-relative plots shown in Figure 9 include maximum mid-level convergence, Z_{DR} column depth, VIL, and 95th percentile Z at -20 ºC. Median maximum mid-level convergence (Figure 9a) shows no signal and remains stagnant through the time window at about 0.003 s^{-1}. Median maximum Z_{DR} column depth (Figure 9b) decreases from roughly 3.2 to 2.7 km

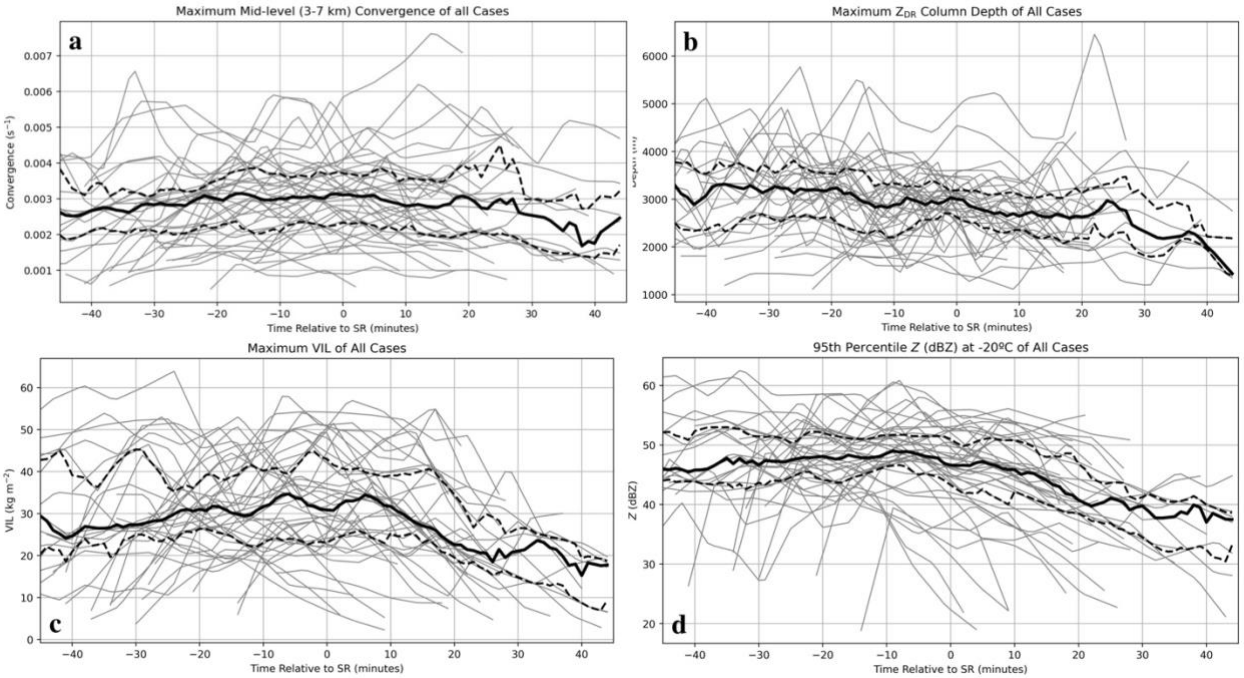

Figure 9. Same as Figure 7, except of a) maximum mid-level convergence (s^{-1}), b) maximum Z_{DR} column depth (m), c) maximum VIL (kg m^{-2}), and d) 95th percentile Z at -20 ºC (dBZ) of all cases.

over the time window, with a slightly more prominent dip in median values near 10 minutes before the SR time likely from storms beginning to collapse. Median maximum VIL (Figure 9c) has two rather prominent peaks of roughly 35 kg m^{-2} at 5 minutes before and 5 minutes after the SR time. The second peak could be due to new updraft growth as some storms cycle. Finally, *Z* at -20 ºC (Figure 9d) has a slight, gradual increase until 5 minutes before the SR time, then begins to decrease as the storm core descends and fewer, smaller hydrometeors exist at the -20 ºC isotherm.

In general, the SR-relative plots using raw data did not produce obvious signals that fit the conceptual model of radar signatures of downburst development. There are a few possible explanations for this, the first being that there are too many outliers or peaks at different times which make the median values more stagnant. Another is that the storms being analyzed are all different sizes. The last reason could be due to the storm's distance from the radar and the effects of beam broadening and poorer resolution that may diminish the magnitude of the observed

signatures compared to what would have been measured closer to the radar. To mitigate these issues, variables were also normalized by the maximum value of each time series in an effort to focus on the temporal evolution of the signals, and it produced a clearer signal for most examined variables.

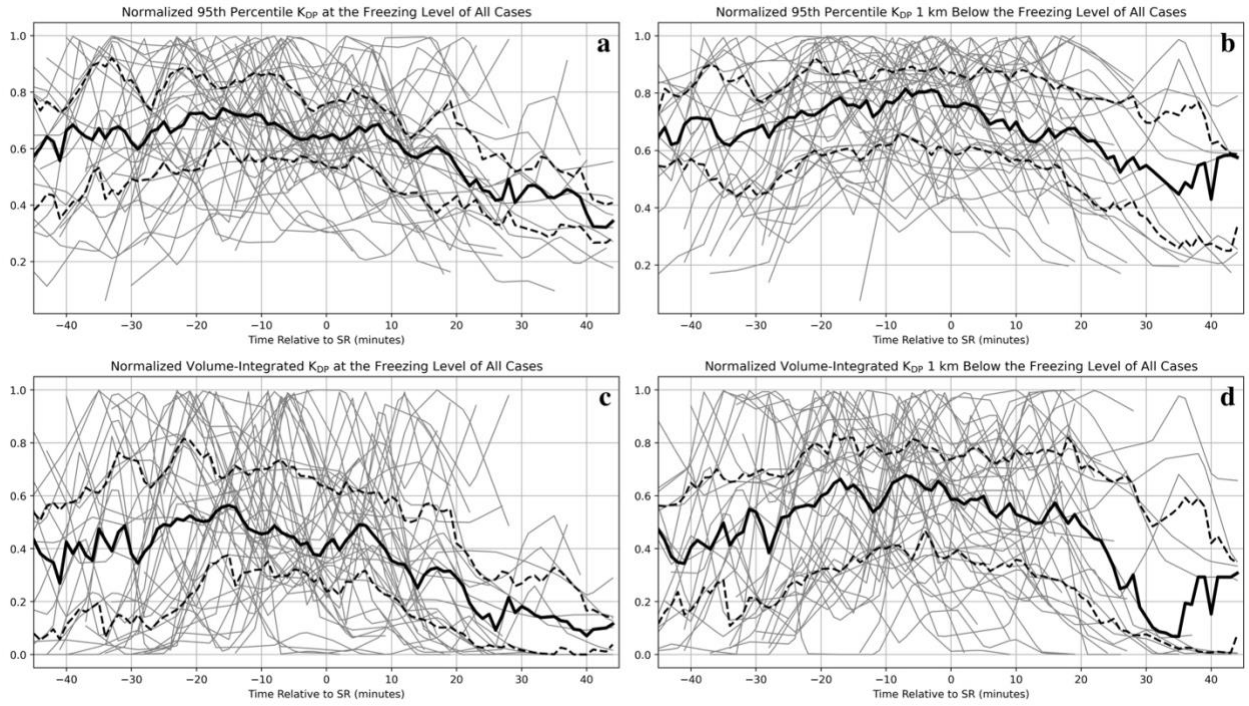

Figure 10. Normalized SR-relative time series of a) 95th percentile K_{DP} at the freezing level, b) 95th percentile K_{DP} 1-km below the freezing level, c) volume-integrated K_{DP} at the freezing level, and d) volume-integrated K_{DP} 1-km below the freezing level. The gray lines represent values of each case, the black dashed lines represent the 25th and 75th percentile values of all cases, and the solid black line represents the median value of all cases.

Starting with the K_{DP}-related plots, normalized 95th percentile K_{DP} (Figure 10a) and volume-integrated K_{DP} (Figure 10c) at the freezing level both peak near 15 minutes before the SR time. Likewise, normalized 95th percentile K_{DP} (Figure 10b) and volume-integrated K_{DP} (Figure 10d) 1-km below the freezing level both peak near 5 minutes before the SR time. This makes sense because the descending K_{DP} core, and therefore the largest values, will pass through the freezing level before passing through 1-km below it. This also agrees with results from Kuster et al. (2021) wherein K_{DP} cores are observed evolving more slowly (about 10 minutes to

descend 1 km in this case) compared to DRCs, which are typically observed within 10 minutes of reaching the surface.

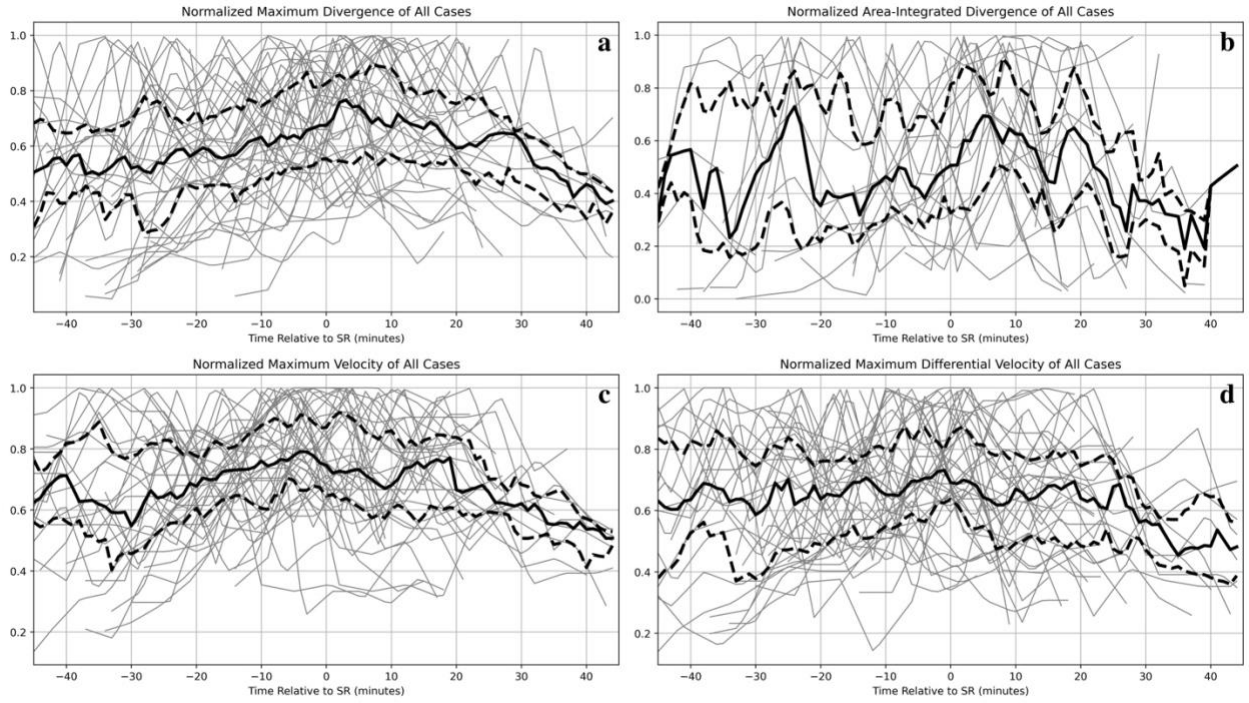

Figure 11. Same as Figure 10, except of a) maximum divergence, b) area-integrated divergence, c) maximum velocity, and d) maximum differential velocity of all cases.

Next, the normalized median values of both the maximum divergence (Figure 11a) and area-integrated divergence (Figure 11b) plots have a large peak 5 minutes after the SR time, which is to be expected since outflow winds near the surface would maximize around the same time damage is reported (i.e., SR time). There is also a large peak near 25 minutes before the SR time on the area-integrated divergence plot, but this is likely due to some storms cycling and producing outflow winds near the surface prior to the downburst event of interest. Median maximum velocity (Figure 11c) values have a small peak near 5 minutes before the SR time, possibly around the time that the downdraft of several storms reaches the surface. Interestingly, the median maximum differential velocity (Figure 11d) is pretty stagnant except for a small peak at the SR time. These time series feature many outliers and peaks at different times, which could be contributing to there being little, if any, signal in the median time series.

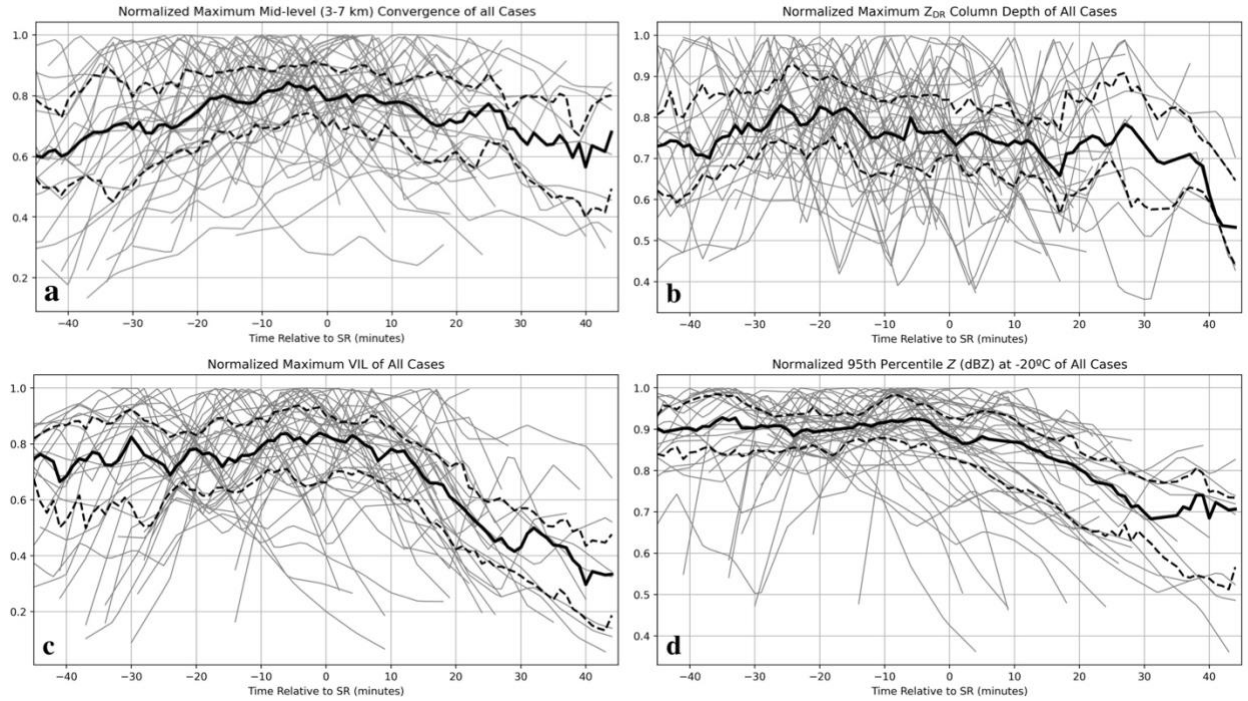

Figure 12. Same as Figure 10, except of a) maximum mid-level convergence, b) maximum Z_{DR} column depth, c) maximum VIL, and d) 95th percentile Z at -20 ºC of all cases.

The last several plots do not show any major signals but do show general trends worth mentioning. The normalized median maximum mid-level convergence (Figure 12a) gradually increases until peaking near 5 minutes before the SR time, then gradually decreasing. This conforms to the conceptual model of mid-level convergence arising due to mass conservation as the downdraft forms and accelerates downward from mid-levels, and also agrees with past studies regarding observed mid-level convergence prior to downburst occurrence (e.g., Isaminger 1988; Roberts and Wilson 1989; Kuster et al. 2016). The median values of maximum Z_{DR} column depth (Figure 12b) only gradually decrease over time, and that of both maximum VIL (Figure 12c) and 95th percentile *Z* at -20 ºC (Figure 12d) only slightly increase until within 5 minutes before the SR time, then quickly decrease. The pattern for 95th percentile *Z* at -20 ºC

supports the presence of DRCs in most cases because the Z core, and therefore the largest Z values, begins collapsing aloft and eventually becomes the DRC in most cases.

After analyzing both the raw and the normalized SR-relative plots, the variables that most distinctly correspond to the downburst at the surface and produce the more prominent signals include normalized maximum divergence, area-integrated divergence, and maximum velocity. Otherwise, the variables that most clearly showed a precursor signature prior to the downburst reaching the surface include normalized 95th percentile and volume-integrated K_{DP} at and 1-km below the freezing level and maximum mid-level convergence. Raw volume-integrated K_{DP} at the freezing level, maximum divergence, maximum velocity, and maximum VIL had small peaks in median values leading up to and at the SR time, but they were much less than prominent than any signals in the normalized plots.

3.2.2 Divergence-signature-relative plots

In the previous section, SR times are used as the anchor times when compositing cases in an effort to incorporate human-reported downburst damage into the analysis. However, during the analysis, it became apparent that they were not always reliable due to either being radar-estimated or reported later than they actually happened (Trapp et al. 2006). These discrepancies led to signals in the median values being smeared as peaks were spread out. To mitigate this uncertainty, surface DS and maximum VIL (MV) times are also explored as anchor times. Surface DS time is determined by plotting velocity and divergence at the lowest PPI tilt and finding the time at which the DS first appears. Similarly, MV time is the time at which the maximum value of VIL occurs within the storm. As with the SR-relative plots, raw and normalized plots are analyzed for both anchor times.

With the uncertainty associated with the SR times removed in favor of a DS based on radar data, the majority of the signals become much more apparent, especially in the normalized plots. Beginning with the raw and normalized plots of 95th percentile K_{DP} at the freezing level, the raw plot (Figure 13a) shows no clear signal until the median values level out at roughly 1.4º km^{-1} from 15 minutes before to 10 minutes after the SR time with a small decrease near the SR time. Conversely, the normalized plot (Figure 14a) median has an obvious peak near 10 minutes before the SR time then decreases. With the raw and normalized plots of 95th percentile K_{DP} 1-km below the freezing level (Figures 13b and 14b, respectively), both median values peak near 5 minutes before the SR time. The peak in the normalized plot is much more pronounced, however.

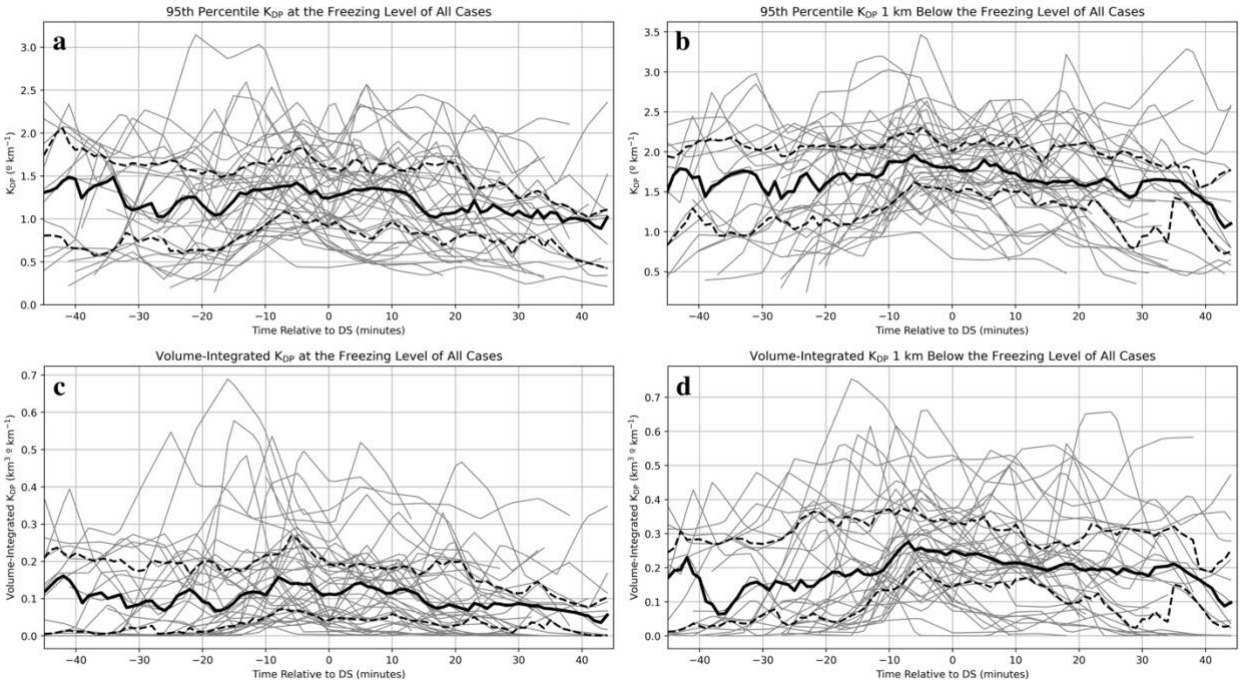

Figure 13. DS-relative time series of a) 95th percentile K_{DP} at the freezing level (º km^{-1}), b) same as a, but at 1-km below the freezing level (º km^{-1}), c) volume-integrated K_{DP} at the freezing level (º km^{-1}), and d) same as c, but at 1-km below the freezing level (º km^{-1}). The gray lines represent values of each case, the black dashed lines represent the 25th and 75th percentile values of all cases, and the solid black line represents the median value of all cases.

Next, raw and normalized volume-integrated K_{DP} at the freezing level (Figures 13c and 14c, respectively) median values peak near 10 minutes before the SR time, with the raw values

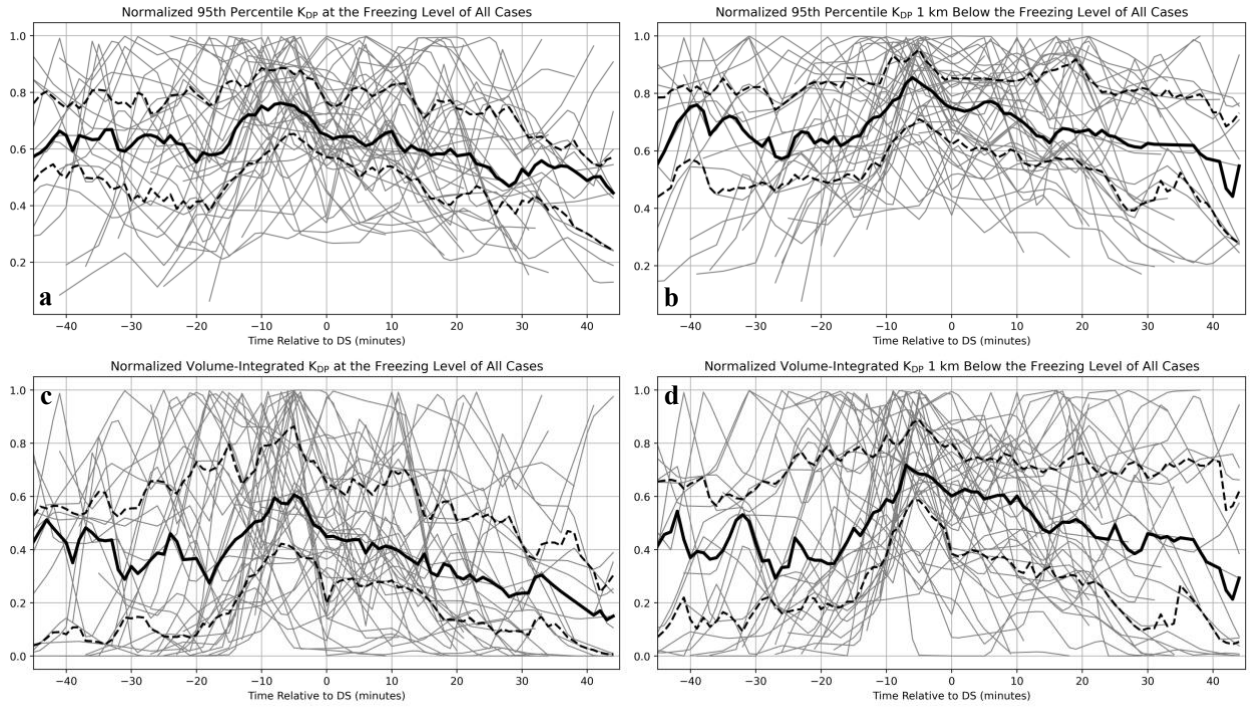

Figure 14. Same as Figure 13, except of normalized a) 95th percentile K_{DP} at the freezing level, b) same as a, but at 1-km below the freezing level, c) volume-integrated K_{DP} at the freezing level, and d) same as c, but 1-km below the freezing level of all cases.

reaching roughly 0.15 º km^{-1} and the peak in the normalized plot being much larger. Raw and normalized volume-integrated K_{DP} 1-km below the freezing level (Figures 13d and 14d, respectively) median values peak within 10 to 5 minutes before the SR time, the raw values reaching roughly 0.3 º km^{-1} and the peak in the normalized plot being much larger again. Furthermore, the 25th and 75th percentile values increase alongside the median values in all of the normalized K_{DP} plots, and they even compress in Figure 13d near the same time as the peak in median values, indicating a strong precursor signature. Overall, for both the raw and normalized plots, the volume-integrated K_{DP} signals were much more pronounced and, similar to the SR-relative plots, they peaked prior to DS time. Unlike the SR-relative plots, however, the evolution time between peaks at the freezing level and 1-km below the freezing level was about 5 minutes.

Next, raw and normalized maximum divergence and area-integrated divergence are investigated. The median values of raw maximum divergence (Figure 15a) gradually increase

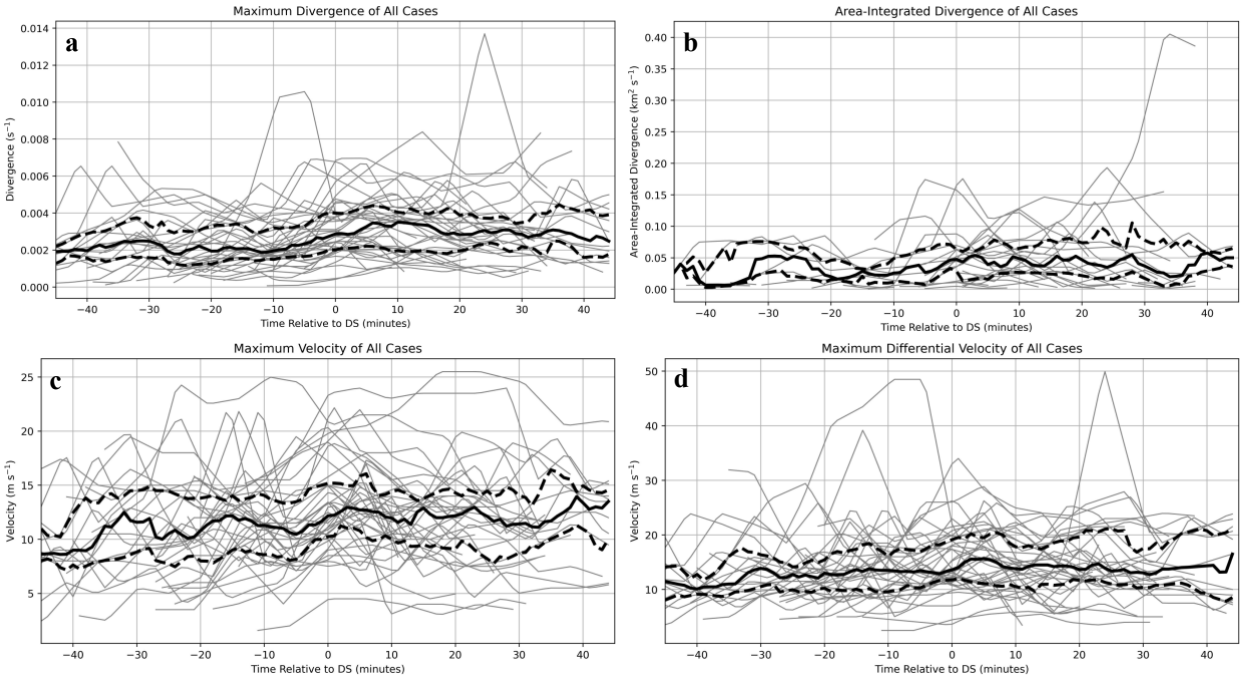

Figure 15. Same as Figure 13, except of a) maximum divergence (s^{-1}), b) area-integrated divergence (s^{-1}), c) maximum velocity (m s^{-1}), and d) maximum differential velocity (m s^{-1}) of all cases.

from 10 minutes before DS time until peaking 5 minutes after the DS time near 0.004 s^{-1} as expected. Normalized median maximum divergence (Figure 16a) values have a large peak from the DS time until 10 minutes later, again as expected. For area-integrated divergence, the raw plot (Figure 15b) has no obvious signals (likely due to there being so few cases that meet the 0.0025 s^{-1} threshold), but the normalized plot (Figure 16b) median values have a large peak starting from 5 minutes before until 10 minutes after the DS time. Moving to the raw and normalized maximum velocity and differential velocity plots, the raw maximum velocity (Figure 15c) plot peaks 5 minutes after the DS time, since winds are expected to peak after the initial appearance of a DS. Normalized maximum velocity (Figure 16c) has a large peak in median values between 5 minutes before to 5 minutes after the DS time, as expected. Median values of both raw and normalized maximum differential velocity (Figures 15d and 16d, respectively) peak 5 minutes after the DS time, again as expected.

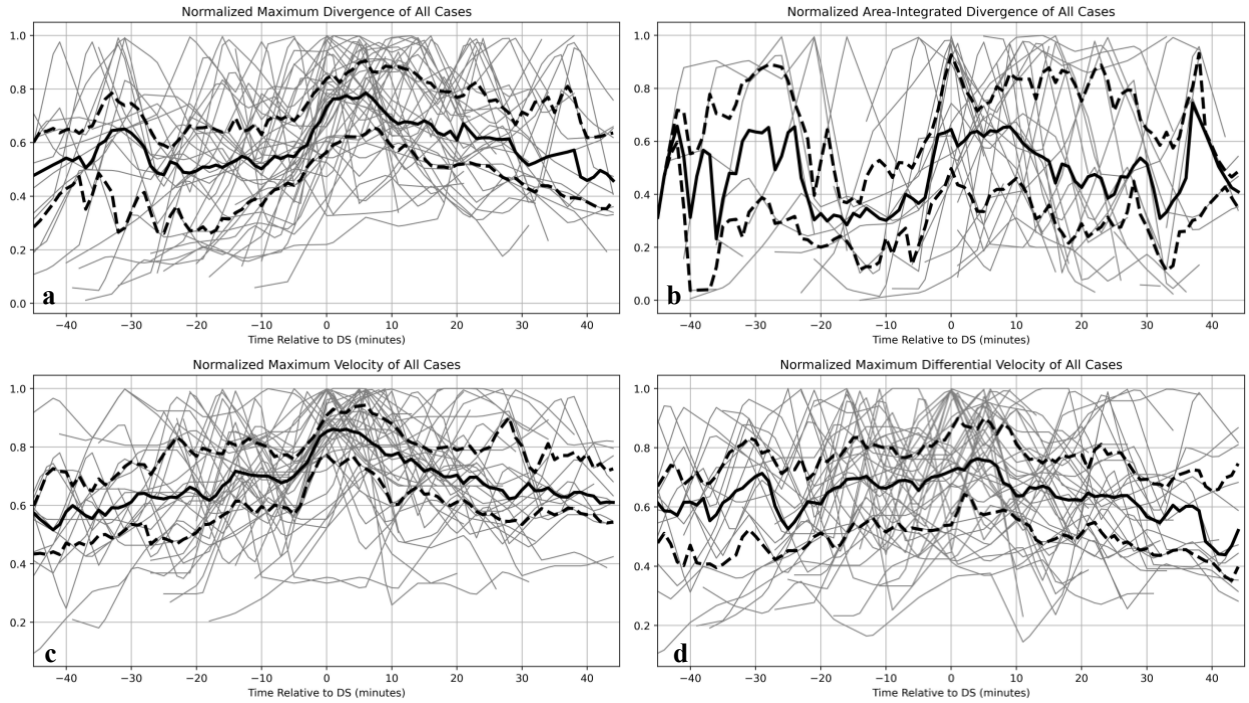

Figure 16. Same as Figure 13, except of normalized a) maximum divergence, b) area-integrated divergence, c) maximum velocity, and d) maximum differential velocity of all cases.

The last several plots of raw and normalized maximum mid-level convergence, Z_{DR} column depth, maximum VIL, and 95th percentile Z at -20 ºC do not have as prominent of signals in their median values but do still show some patterns as expected. The normalized maximum mid-level convergence (Figure 18a) has median values that increase until the DS time starting roughly 20 minutes beforehand. The plots of raw maximum mid-level convergence (Figure 17a) and maximum Z_{DR} column depth (Figure 17b) show no obvious signals, but the median values of maximum Z_{DR} column depth do gradually decrease through the time window. The normalized Z_{DR} column depth plot (Figure 18b) is similar to its raw counterpart, but the median values do have a slight peak near 15 minutes before the DS time, possibly when storms in several cases begin to collapse. In both raw (Figure 17c) and normalized (Figure 18c) maximum VIL plots, the median values peak just after the DS time following a gradual increase, then begin to decrease, indicative of the core of precipitation finally reaching the surface accompanying the downburst and being removed from the system. Lastly, the raw and normalized plots of 95th percentile Z at -

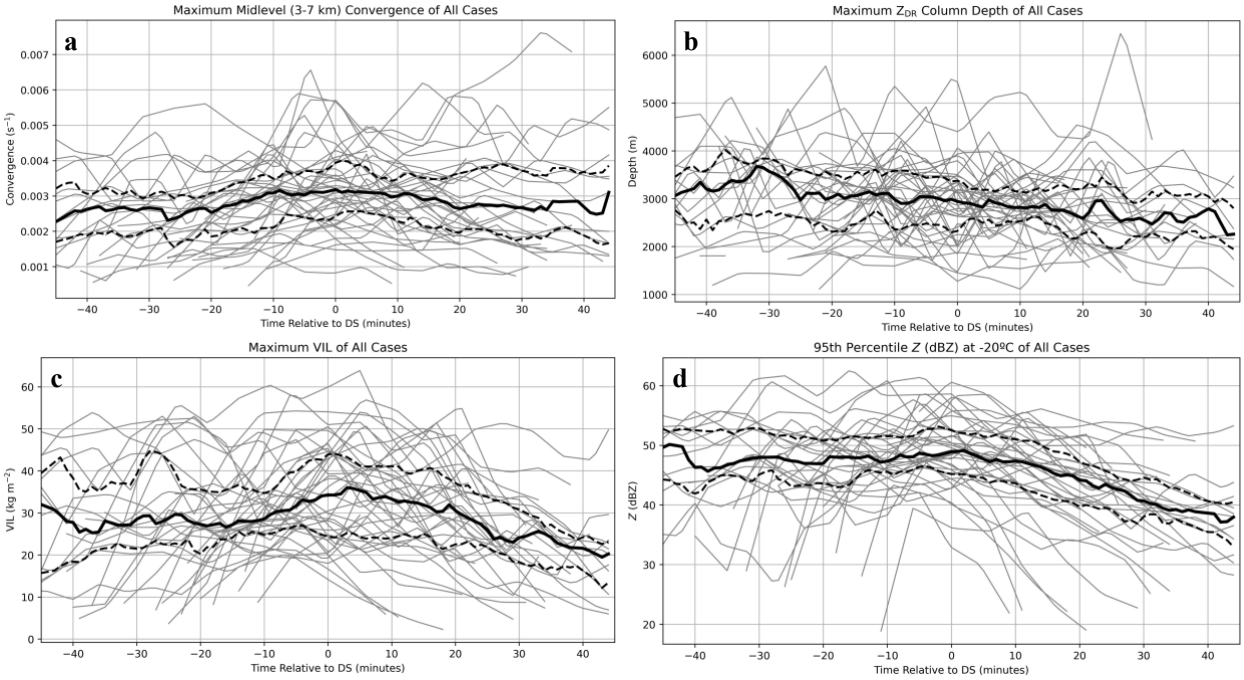

Figure 17. Same as Figure 13, except of a) maximum mid-level convergence, b) maximum Z_{DR} column depth, c) maximum VIL, and d) 95th percentile Z at -20 ºC of all cases.

20 ºC (Figures 17d and 18d, respectively) also show no obvious precursor signal. The median values in the raw plot are stagnant until 5 minutes after the DS time, and those in the normalized plot are stagnant until 5 minutes before the DS time, after which both begin to dramatically decrease. In the same way this was expected for the SR-relative plots, it is also expected with DS-relative plots as DRCs evolve.

Overall, the DS-relative plots showed much clearer and more prominent signatures in almost all variables compared to the SR-relative plots. Variables that most distinctly correspond to the downburst at the surface and produce the more prominent signals include maximum and area-integrated divergence and maximum velocity and differential velocity. Otherwise, the variables that most clearly showed a precursor signature prior to the downburst reaching the surface include the raw volume-integrated K_{DP} 1-km below the freezing level, all normalized K_{DP}-related variables, and normalized maximum mid-level convergence and VIL.

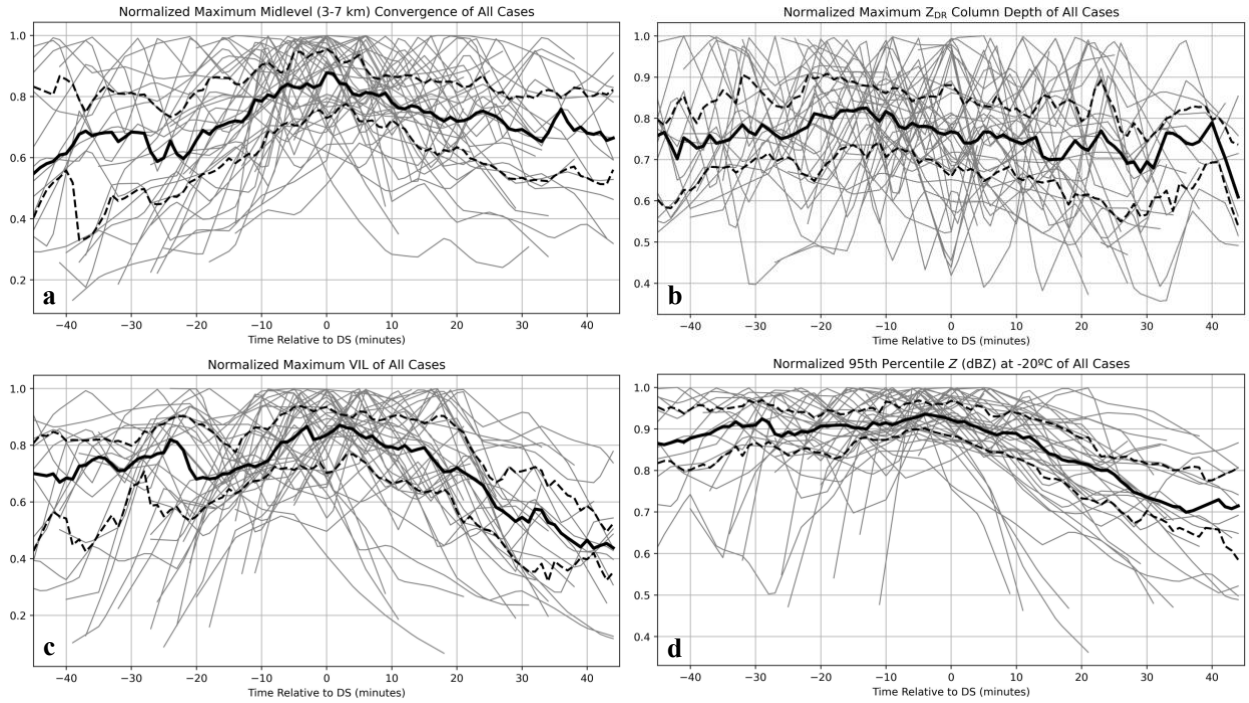

Figure 18. Same as Figure 13, except of normalized a) maximum mid-level convergence, b) maximum Z_{DR} column depth, c) maximum VIL, and d) 95th percentile Z at -20 ºC of all cases.

3.2.3 Maximum-VIL-relative plots

The final group of plots investigated are the raw and normalized MV-relative plots, which use the time at which VIL reaches its maximum within a storm as the anchor time. This variable was chosen to be investigated as a possible proxy for when the storm was at its most intense. Surprisingly, this anchor time did not produce any major signals in any raw or normalized plots, so most are not shown for brevity.

Median values of the raw and normalized 95th percentile *Z* at -20 ºC (Figures 19d and 20d, respectively) have a small peak right before the MV time then gradually decrease, which follows because as VIL maximizes (at the MV time), *Z* will also maximize, especially aloft where ice particles are present. The only other plot depicting a small downburst signal includes normalized maximum mid-level convergence (Figure 20a), which peaks at the MV time. Otherwise, the median values of normalized 95th percentile and volume-integrated K_{DP} at the

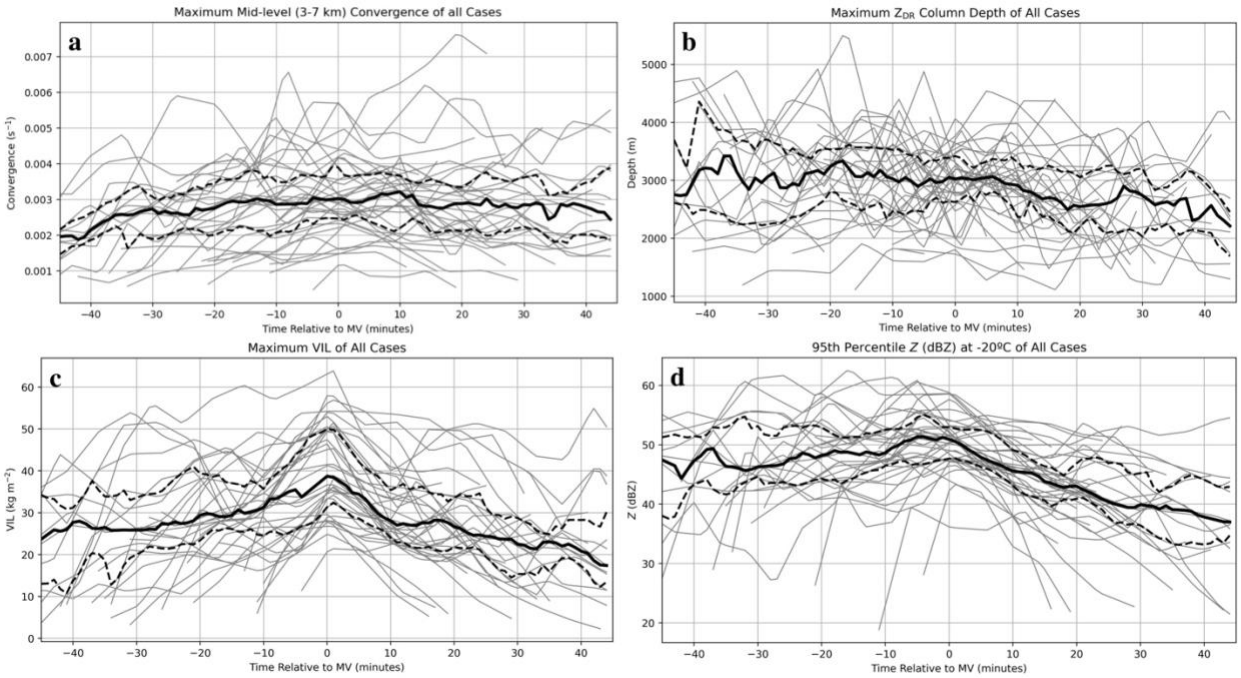

Figure 19. MV-relative time series of a) maximum mid-level convergence (s^{-1}), b) maximum Z_{DR} column depth (m), c) maximum VIL (kg m^{-2}), and d) 95th percentile Z at -20 ºC (dBZ). The gray lines represent values of each case, the black dashed lines represent the 25th and 75th percentile values of all cases, and the solid black line represents the median value of all cases.

freezing level remain almost stagnant until the MV time. Likewise, the median values of normalized 95th percentile and volume-integrated K_{DP} 1-km below the freezing level remain nearly stagnant until 5 minutes after the MV time, which makes sense temporally. The median values of maximum VIL (Figure 20c) peaked at the MV time, as expected. The rest of the variables investigated, however, did not show any prominent signals. Overall, given that far fewer variables display a clear downburst signature compared to the SR- and DS-relative plots, it can be inferred that the MV-relative plots are not a representative anchor time to use for analysis.

3.2.4 Occurrence statistics

The previous section's results indicate that while many cases had certain signatures preceding downburst occurrence, the exact timing of them with respect to the anchor time often varied, making a mean time series hard to decipher. To address this, Table 1 summarizes the

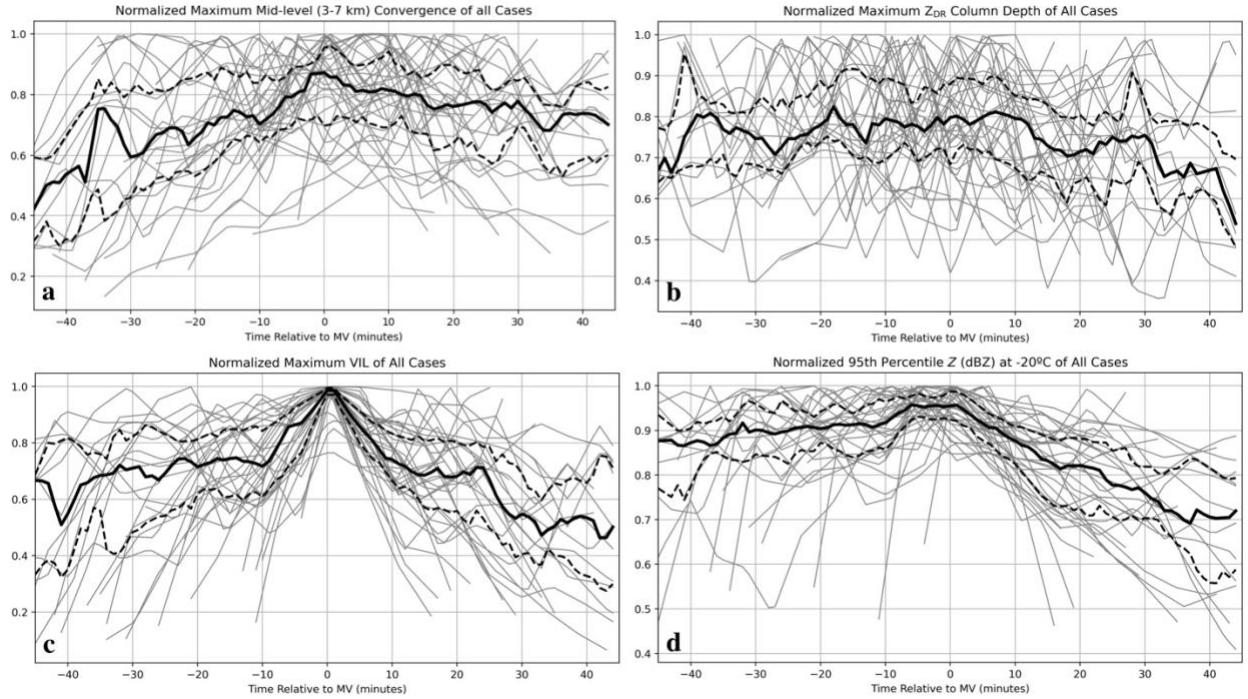

Figure 20. Same as in Figure 19, except of normalized a) maximum mid-level convergence (s^{-1}), b) maximum Z_{DR} column depth (m), c) maximum VIL (kg m^{-2}), and d) 95th percentile Z at -20 ºC (dBZ) of all cases.

occurrence frequency statistics of each examined variable and investigates the differences, if any, by geographic region. It should be noted that some regions have a limited number of cases, so the observed frequencies may not be totally representative of the region (such as the Northeast, which only has 4 cases). For each variable, the ratio of cases in each region and in total that meet a certain threshold is given, without respect to any anchor time. First, the 95th percentile K_{DP} at and 1 km below the freezing level are analyzed to see if they meet a K_{DP} core threshold of 1 º km^{-1} (Kuster et al. 2021). At both heights, a majority of the cases in all regions reach this threshold. The number of cases in the Southwest that reach this threshold at the freezing level is a bit lower than the rest of the regions (0.78 cases), possibly because of climatologically drier conditions promoting more evaporation and therefore less total liquid mass, but in general this is only a few cases less than the rest of the regions. With the exception of one or two cases, this threshold is met in every case 1 km below the freezing level, likely due to hydrometeors beginning to melt and the mass of liquid increasing there.

Next, all cases in the Southwest reach a maximum mid-level convergence and low-level divergence threshold of 0.0025 s^{-1} (Dance and Potts 2002; Wilson et al. 1984) and all cases in the Northeast reach the threshold for maximum mid-level convergence. The majority of cases in the Midwest and Southeast also reach the threshold for maximum mid-level convergence, and the majority of cases in the Southeast also reach the threshold for maximum low-level divergence. Similar results were found in research done by Isaminger (1988) wherein mid-level convergence was much less frequently observed in the Southeast compared to the Plains. A majority of cases in the Midwest, however, do not meet the threshold for maximum low-level divergence, and only half of the cases in the Northeast meet this threshold. In total, maximum mid-level convergence and low-level divergence do reach 0.0025 s^{-1} in most cases, but maximum low-level divergence does so less frequently. A possible explanation for this is sparse radar coverage at or near the surface in cases where storms are farther away from the radar, thereby underestimating divergence values. It is also possible that environments are not as supportive of thermally driven downdrafts (especially in the Southeast and Northeast where the 0–2-km LR remain under 8 ºC km^{-1} in a majority of cases), so precipitation loading is the main forcing mechanism and outflow winds enhanced by the resultant thermal buoyancy density gradient near the surface may not spread as prominently. Conversely, in the Southwest where 0–2-km LR are above 8 ºC km^{-1} in 72% of cases, downdrafts may be more thermally driven which is why low-level divergence reaches 0.0025 s^{-1} in all cases.

Surprisingly, maximum velocity and differential velocity in nearly all cases rarely met the thresholds of 25 m s^{-1} and 40 m s^{-1} (Smith et al. 2004), respectively. No cases in the Northeast reached either threshold, and very few reached it in the remaining regions, causing totals to be low as well (just 0.20). It is worth noting that in the Southwest and Midwest, any cases that met

one criterion (i.e., 25 m s^{-1} maximum velocity) also met the other (e.g., 40 m s^{-1} maximum differential velocity). The unexpectedly low number of cases that reach these thresholds could again be due to storm distance from radar and poorer coverage but Smith et al. (2004) point out that radar-based wind speeds are often underestimated, even with

Table 1. Summary of occurrence frequency statistics for all downburst cases divided by the same regions in Figure 2 (18 in the Southwest, 6 in the Midwest, 13 in the Southeast, and 4 in the Northeast) and total (41) which meet a certain threshold. Values given are the ratio of cases that meet the threshold to the total number of cases. Bold frequencies are those which occurred in 0.75 or more cases.

	Southwest	Midwest	Southeast	Northeast	Total
95th percentile K_{DP} at freezing level > 1 º km^{-1}	**0.78**	**1.0**	**0.92**	**1.0**	**0.88**
95th percentile K_{DP} 1–km below freezing level > 1 º km^{-1}	**0.94**	**1.0**	**1.0**	**1.0**	**0.98**
Maximum mid-level convergence > 0.0025 s^{-1}	**1.0**	0.67	0.69	**1.0**	**0.85**
Maximum low-level divergence > 0.0025 s^{-1}	**1.0**	0.33	0.69	0.50	**0.76**
Maximum velocity > 25 m s^{-1}	0.22	0.17	0.23	0.0	0.20
Maximum differential velocity > 40 m s^{-1}	0.22	0.17	0.15	0.0	0.17
Maximum Z_{DR} column depth > 3 km	**0.83**	**1.0**	**0.85**	**1.0**	**0.88**
Maximum VIL > 30 kg m^{-2}	**0.89**	0.17	**0.77**	**1.0**	**0.76**
95th percentile Z at -20ºC > 50 dBZ	0.72	0.17	0.69	**0.75**	0.63
0–2 km LR > 8º km^{-1}	0.72	0.67	0.46	0.25	0.71
WINDEX > 60	0.61	0.17	0.31	0.0	0.39

better low-level coverage. There is also no consensus on which velocity and differential velocity thresholds define a downburst, and several prior studies use a much-less-stringent threshold of 10 m s^{-1} for differential velocity to define downbursts (e.g., Wilson et al. 1984). The thresholds used in this study may just be larger than typical downburst values given that they are used in Smith et al. (2004) to define severe from non-severe downbursts.

Maximum Z_{DR} column depth, VIL, and 95th percentile Z at -20 ºC were explored next, seeing if cases would reach thresholds of 3 km (Snyder et al. 2015), 30 kg m^{-2} (Kitzmiller et al. 1995), or 50 dBZ, respectively. Maximum Z_{DR} column depth reached 3 km in a majority of cases overall (0.88), the fewest being in the Southwest, although a majority of cases still reached it there (0.83). A maximum VIL of 30 kg m^{-2} was reached in a majority of cases overall (0.76), with the exception of the Midwest, where just 17% of cases met this threshold. All but one case in the Midwest occurred in environments with 0–4-km LR below 7.13º km^{-1}, so storm updrafts in these cases may not be very strong and there may be less liquid within them (Kitzmiller et al. 1995). Similarly, the threshold for 95th percentile Z at -20 ºC is met in a majority of cases (0.63), but only 0.17 cases meet it in the Midwest. Again, this is possibly due to weaker updrafts which produce either fewer or smaller hydrometeors aloft, causing smaller Z values.

Lastly, the environmental parameters 0–2-km LR and WINDEX are explored. The thresholds used are 8 ºC km^{-1} (Srivastava 1985) and 60 (McCann 1994), respectively. In the majority of cases, the LR threshold was met (0.71 cases), but less than half of the cases in the Southeast met this threshold and only 0.25 cases met it in the Northeast. For the Southeast, near-coastal Northeast (NY and NJ), and farther south Northeast (PA) cases, this could potentially be due to higher moisture in the 0–2-km AGL layer based on terrain and climatology which would prevent temperatures from decreasing with height as rapidly as they would in a drier region, such as the Southwest. The threshold for WINDEX was reached most in the Southwest (0.61 cases) and was reached least in the Midwest (0.17 cases) and Northeast (0 cases). One possible explanation for this is that the equation for WINDEX is weighted rather heavily by the surface-to-freezing-level LR, which is typically largest in the Southwest and smaller in the Midwest and Northeast. Results from Romanic et al. (2022) are similar in that the Southwest and Plains

regions, where WINDEX values of cases in this study most frequently reach 60 or higher, had the most severe downburst potential.

Frequencies of 0.75 or greater are bolded in Table 1 to show which variables reached their respective threshold in almost all cases for each region and in total. For total cases and for the Southwest cases, this included 95th percentile K_{DP} at and 1-km below freezing level, mid-level convergence, low-level divergence, maximum Z_{DR} column depth, and maximum VIL. For the Midwest cases, this included 95th percentile K_{DP} at and 1-km below freezing level and maximum Z_{DR} column depth. For the Southeast cases, this included 95th percentile K_{DP} at and 1-km below freezing level, maximum Z_{DR} column depth, and maximum VIL. Finally, for the Northeast region this included 95th percentile K_{DP} at and 1-km below freezing level, mid-level convergence, maximum Z_{DR} column depth, maximum VIL, and 95th percentile Z at -20 ºC.

Complementary to Table 1, additional quantitative analysis is done by creating cumulative frequency distributions (CFD) of each storm variable in all cases (Figure 21) and regional cases (not shown). The median values from the national CFD are compared to those from each regional CFD as well. Starting with the CFD of all cases, low-level divergence (Fig. 21d), mid-level convergence (Fig. 21c), and maximum differential velocity (Fig. 21f) do not have a Gaussian distribution, as shown by the longer "tails" at higher values, meaning that most cases have rather low values, but a few others may have anomalously high values. On the other hand, the rest of the variables do have a near-Gaussian distribution, speaking to the variability of the values across the U.S.

Starting with the 95th percentile K_{DP} at the freezing level (Figure 21a), the median across all cases is 1.85 º km^{-1}. The Southwest region is the only one whose median falls below the national median at 1.75 º km^{-1}, while the Southeast has the same median value, and the Midwest

and Northeast regions have higher-than-national median values at 1.88 º km^{-1}and 2.61 º km^{-1}, respectively. Similarly, for 95th percentile K_{DP} 1 km below the freezing level (Figure 21b), the Southwest and Southeast regions have median values below the national median of 2.38 º km^{-1} at 2.23 and 2.27 º km^{-1}, respectively, while the Midwest and Northeast regions have values above the national median at 2.49 º km^{-1} and 2.65 º km^{-1}, respectively.

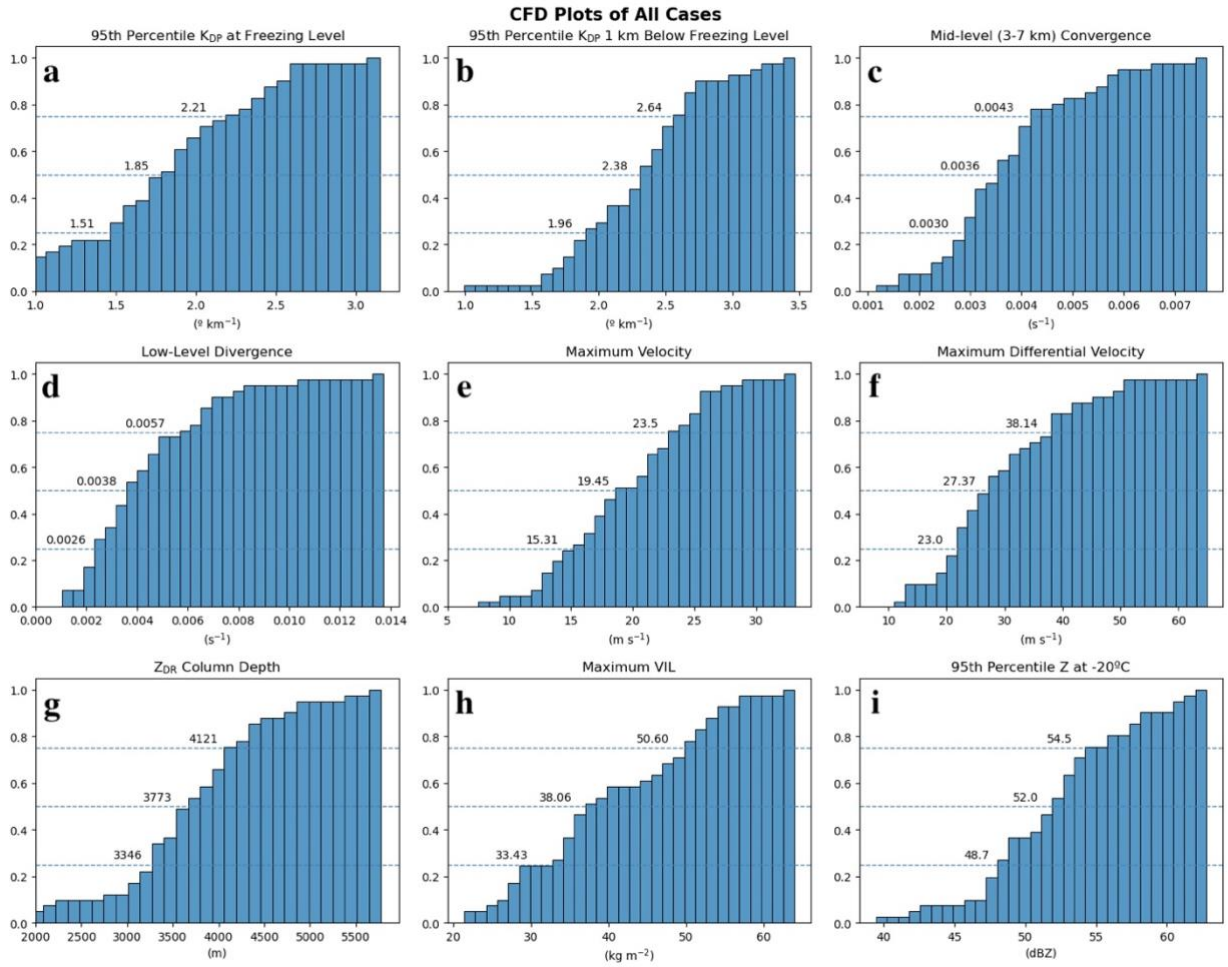

Figure 21. Cumulative frequency distribution plots of all cases for all variables. The top dashed line marks the 75th percentile, the middle dashed line marks the median, and the bottom dashed line marks the 25th percentile.

The median maximum mid-level convergence of all cases (Figure 21c) is 0.0036 s^{-1}. This is above the median values of the Midwest (0.0030 s^{-1}), Southeast (0.0033 s^{-1}), and Northeast regions (0.0034 s^{-1}), but below the Southwest median value of 0.0042 s^{-1}. The maximum low-level divergence (Figure 21d) exhibits a similar pattern with a median value of 0.0038 s^{-1} across

all cases, higher than the Midwest (0.0023 s^{-1}) and Northeast (0.0024 s^{-1}) region median values and matching the Southeast region median value. The Southwest region is again above the national median at 0.0044 s^{-1}. The median maximum velocity (Figure 21e) and differential velocity (Figure 21f) values for all cases are 19.45 m s^{-1} and 27.37 m s^{-1}, respectively. Median values in the Southwest region are both above the national median at 21.55 m s^{-1} for maximum velocity and 31.49 m s^{-1} for maximum differential velocity, and values are below the national median in the Southeast (17.5 m s^{-1} and 27.0 m s^{-1}, respectively) and Midwest (14.11 m s^{-1} and 19.50 m s^{-1}, respectively) regions. The median maximum velocity in the Northeast region is above the national median at 20.75 m $s^{-1}$and median maximum differential velocity is below the national median at 23.75 m s^{-1}.

Next, the national median maximum Z_{DR} column depth (Figure 21f) is 3773 m, which is slightly above the Southeast and Southwest regional median values of 3552 m and 3643 m, respectively, and below the Midwest and Northeast regional median values of 3900 m and 4144 m, respectively. Finally, the median maximum VIL (Figure 21g) and 95th percentile Z at -20 ºC (Figure 21h) values across all cases are 38.06 kg m^{-2} and 52.0 dBZ, respectively. The Southeast, Southwest, and Northeast regional median values are all above the national median at 38.83 kg m^{-2}, 40.53 kg m^{-2}, and 48.58 kg m^{-2}, respectively, and 52.2 dBZ, 52.6 dBZ, and 56.7 dBZ, respectively, while the Midwest median value falls below the national median at 28.02 kg m^{-2} and 48.4 dBZ, respectively.

To summarize, downburst cases in the Southwest region typically had lower K_{DP} values in general, but higher values of wind-related variables as well as more favorable environmental conditions. On the other hand, cases in the Midwest typically had higher K_{DP} values, but were generally weaker given that the thresholds for divergence, velocity, and VIL were often not met.

WINDEX values were also lower here, though 0–2-km LR tended to be close to the threshold of 8 ºC km^{-1}. Southeast and Northeast cases were similar in that both typically had higher K_{DP} values and tended to be stronger. However, cases in the Southeast had higher values of wind-related variables, Z_{DR} column depth, and VIL, whereas those in the Northeast did not have high values of wind-related variables. In both regions, the environment tended to be less favorable as well.

3.3 Comparing variable time series based on geographic location and environmental conditions

The last step of analysis is comparing raw variable time series when split up based on geographic location (eastern versus western U.S.) and environmental conditions (WINDEX greater than versus less than 60 and 0-2 km LR greater than versus less than 8º km^{-1}). These conditions are chosen to investigate any geographic variability, any differences in downburst intensity based on temperature LR (Srivastava 1985; 1987), and because WINDEX has been shown to be related to potential downburst intensity (Romanic et al. 2022). To do so, all cases are split into groups based on these conditions and the median time series and interquartile range of each variable are plotted relative to DS time. DS is chosen as the anchor point for these plots because there are clearer signatures and precursors in the DS-relative plots for all cases, and they were more consistent than the SR- or MV-relative plots.

3.3.1 Geographic region (east versus west) comparison

Figure 22 shows a comparison of the time series of each examined variable separated into western (red) and eastern (blue) regions. The shaded areas represent the interquartile ranges of

the time series distributions at each time and the solid line represents the median. The cases were split up based on their position relative to the Mississippi River so that cases in Alabama, South Carolina, New York, New Jersey, Florida, Maine, Ohio, Kentucky, Georgia, Tennessee, and Pennsylvania comprise the eastern cases and cases in Texas, Oklahoma, Kansas, and Arizona comprise the western cases. For all variables, the time window considered for a signature to be a downburst precursor is from 30 minutes prior to 10 minutes after the DS time.

Area-integrated divergence (Figure 22a) of both regions spikes within 5 minutes after the DS time, which is to be expected. Western cases peak quite a bit higher than eastern cases, likely either because the integrated area of western storms is typically larger than eastern storms based on radar observations, or the downbursts themselves were just stronger in general. Next, the volume-integrated K_{DP} at (Figure 22b) and 1-km below (Figure 22c) the freezing level both have median values which are generally lower in the west. Western cases also peak near DS time, whereas eastern cases peak around 5 minutes before DS time at both heights. Values of the 95th percentile K_{DP} at (Figure 22d) and 1 km below (Figure 22e) the freezing level are similar to the volume-integrated K_{DP} values, peaking about 10 minutes before the DS time in eastern cases and right at the DS time in western cases 1 km below the freezing level. At the freezing level, western cases have a slight peak near 10 minutes before the DS time and eastern cases peak about 5 minutes before the DS time, and values of western cases are generally less than eastern cases again. Two possible theories for why western storms exhibit lower K_{DP} values at and below the freezing level are that (1) less precipitation loading is needed to initiate downbursts due to more favorable thermodynamic environments (e.g., Kuster et al. 2021), and/or (2) the inclination for eastern storms to produce smaller hail (Allen and Tippett 2015), which can accumulate surface meltwater and form oblate meltwater tori near and below the freezing level, greatly

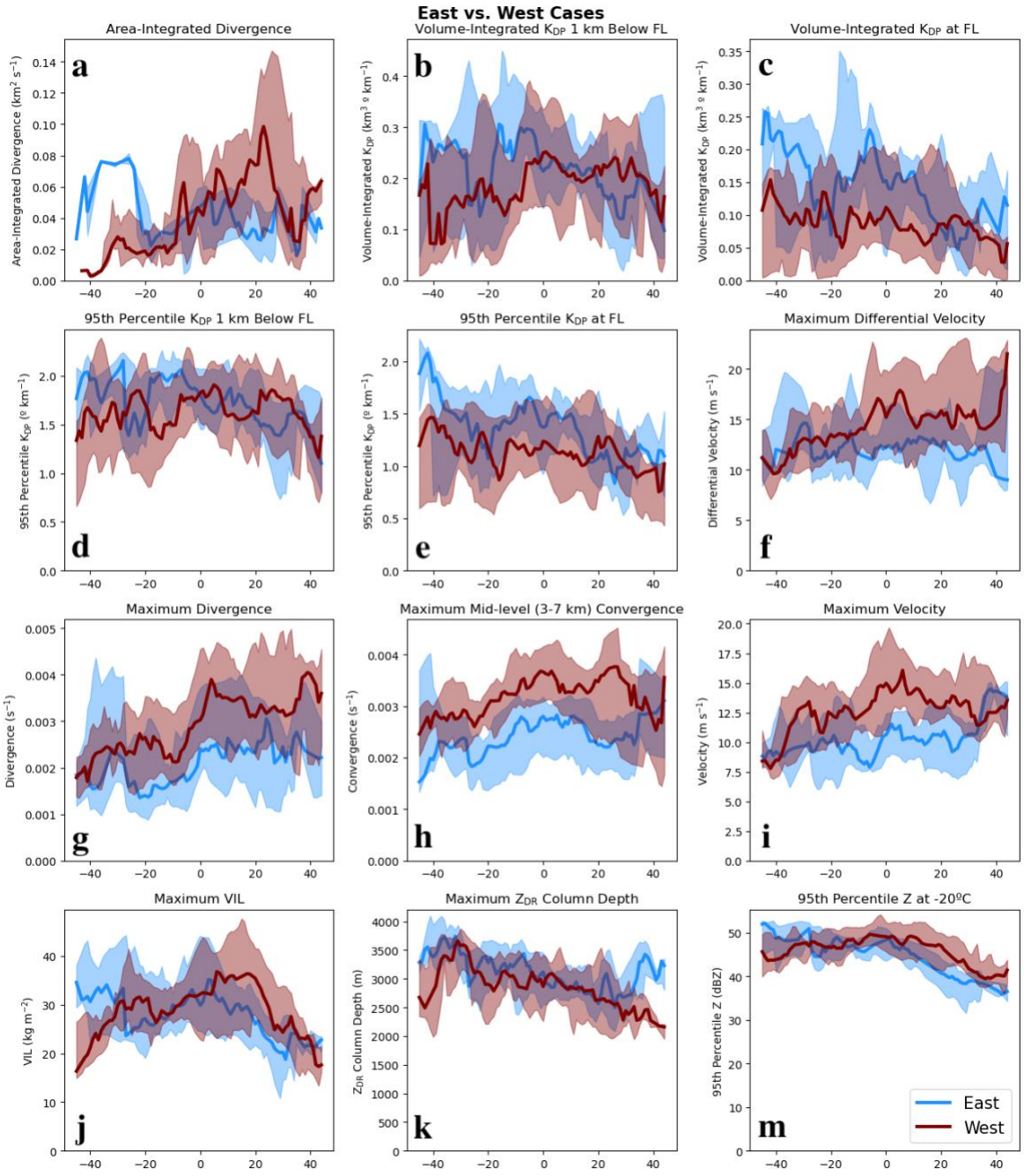

Figure 22. DS-relative 25th percentile, median, and 75th percentile time series plots of cases in the western U.S. (red line, shaded) and the eastern U.S. (blue line, shaded) for all variables of interest.

increasing K_{DP} values there (Kumjian et al. 2019), while larger hail tends to shed its meltwater below the freezing level.

The maximum velocity (Figure 22i) and maximum differential velocity (Figure 22f) plots are rather similar in that they both overlap quite a bit within the time window. Both eastern and

western cases have a peak near 10 minutes after DS time in maximum differential velocity, and both regions have a peak at DS time in maximum velocity, as is expected. Following DS time in eastern maximum differential velocity, there is a slightly larger separation between the values and the western cases peak just over 5 m s^{-1} higher than eastern cases. The difference between peaks of the maximum velocity is not as large, but western case values are still consistently above eastern case values. In addition, the maximum mid-level convergence (Figure 22h) and low-level divergence (Figure 22g) plots show similar patterns in that the median values are completely separate throughout the time window, with western-storm values consistently higher than those of eastern storms.

Maximum VIL (Figure 22j) is the last plot that shows any major differences between the two regions, with eastern case median values gradually increasing starting about 30 minutes before the DS time and peaking right after the DS time, whereas western case median values start increasing nearly 20 minutes before the DS time and peak almost 10 minutes after the DS time. The western case median values are generally higher than those of eastern cases during most of the time window. An interesting feature to note is that western cases also peak about 5 to 10 minutes later than the eastern cases relative to DS time. The eastern and western values in the final two plots, maximum Z_{DR} column depth (Figure 22k) and 95th percentile Z at -20ºC (Figure 22m), are quite similar throughout the time window with only small differences between them. For the median maximum Z_{DR} column depth, eastern and western cases generally decrease over time and the median values of eastern cases are just barely larger than those of western cases. The median 95th percentile Z at -20 °C follow similar patterns in both regions, gradually increasing until the DS time then decreasing after. The median values of both regions are nearly the same as well.

Overall, these plots show rather similar patterns for most of the variables in each region and within the time window. Median values of low-level divergence, mid-level convergence, maximum velocity, area-integrated divergence, maximum VIL, maximum Z_{DR} column depth, and 95th percentile Z at -20 ºC in eastern and western cases all follow a similar evolution compared to each other, and for low-level divergence, mid-level convergence, and maximum velocity, values for western cases are consistently larger than those in eastern cases. Otherwise, median values of volume-integrated and 95th percentile K_{DP} at and 1-km below the freezing level in eastern cases peaked above those in western cases within 10 minutes of the DS. Maximum differential velocity is similar except that its median values in western cases peaked above those in eastern cases at the DS time.

3.3.2 Environmental condition (WINDEX and 0-2 km LR) comparisons

The next two sets of plots were separated based on their calculated WINDEX values (Figure 23) for one set and their calculated 0–2-km LR values (Figure 24) for the second set. The WINDEX plots are split based on whether a case had a value over 60 (O60) versus under 60 (U60), and the 0–2-km LR plots are split based on whether a case had a value over (O8) versus under 8º km^{-1} (U8). Both sets of plots are shown, but the WINDEX plots are the focus of discussion because they are exceedingly similar since LR is a strong component of the equation for WINDEX. Most cases that reach WINDEX values over 60 are from the Southwest region (12) along with 3 Southeast and 1 Midwest case; likewise, most cases that reach 0–2-km LR values over 8 ºC km^{-1} are from the Southwest region (7) along with 1 Midwest case.

Starting with the K_{DP}-related plots, U60 median values were larger than those of O60 in all plots. At the freezing level, median volume-integrated K_{DP} in O60 (Figure 23c) cases peaks

nearly 15 minutes before the DS time at roughly 0.20 º km^{-1}, and nearly 5 minutes before the DS time at roughly 0.10 º km^{-1} in the U60 (Figure 23c) cases. The same plots for 95th percentile K_{DP} at the freezing level are similar except that O60 (Figure 23e) cases peak at 5 minutes before the DS time. At 1 km below the freezing level, the median values of the U60 cases are generally larger than those of O60 again, though not by as much as at the freezing level. For volume-integrated K_{DP}, O60 and U60 (Figure 23b) both peak near 5 minutes before the DS time reaching nearly 0.30 º km^{-1} in U60 cases. As for 95th percentile K_{DP} here, U60 (Figure 23d) cases generally decrease, but have no obvious signal, and O60 (Figure 23d) cases peak near 5 minutes before the DS time at roughly 2º km^{-1}. Another common trait is O60 median values starting at or near 0 º km^{-1} for all volume-integrated K_{DP} plots and at or near 0.5º km^{-1} for all 95th percentile K_{DP} plots, all followed by a rapid increase. All of the U60 cases having higher K_{DP} values than O60 may again be due to precipitation loading being the main downdraft forcing mechanism, since lapse rates are lower in both, which aligns with the hypothesis of Kuster et al. (2021). These higher K_{DP} values are evidence of the higher precipitation amounts needed to generate a downburst in less favorable environments with more stable LR.

Looking at divergence (Figure 23g) next, U60 has no obvious peaks and only gradually increases from 10 minutes before to 10 minutes after the DS time, whereas O60 peaks near 5 minutes after the DS time with values up to 0.004 s^{-1}. For area-integrated divergence (Figures 23a) and maximum velocity (Figures 23i), all cases had similar median values, and all generally increase then peak just after the DS time. Median values of maximum differential velocity in O60 cases (Figure 23f) peak at the DS time, reaching just over 15 m s^{-1}, whereas those in U60 have no clear signal. Lastly, median values of maximum mid-level convergence (Figure 23h) for O60 cases peaks at the DS time and the U60 cases have a small peak near 5 minutes before the

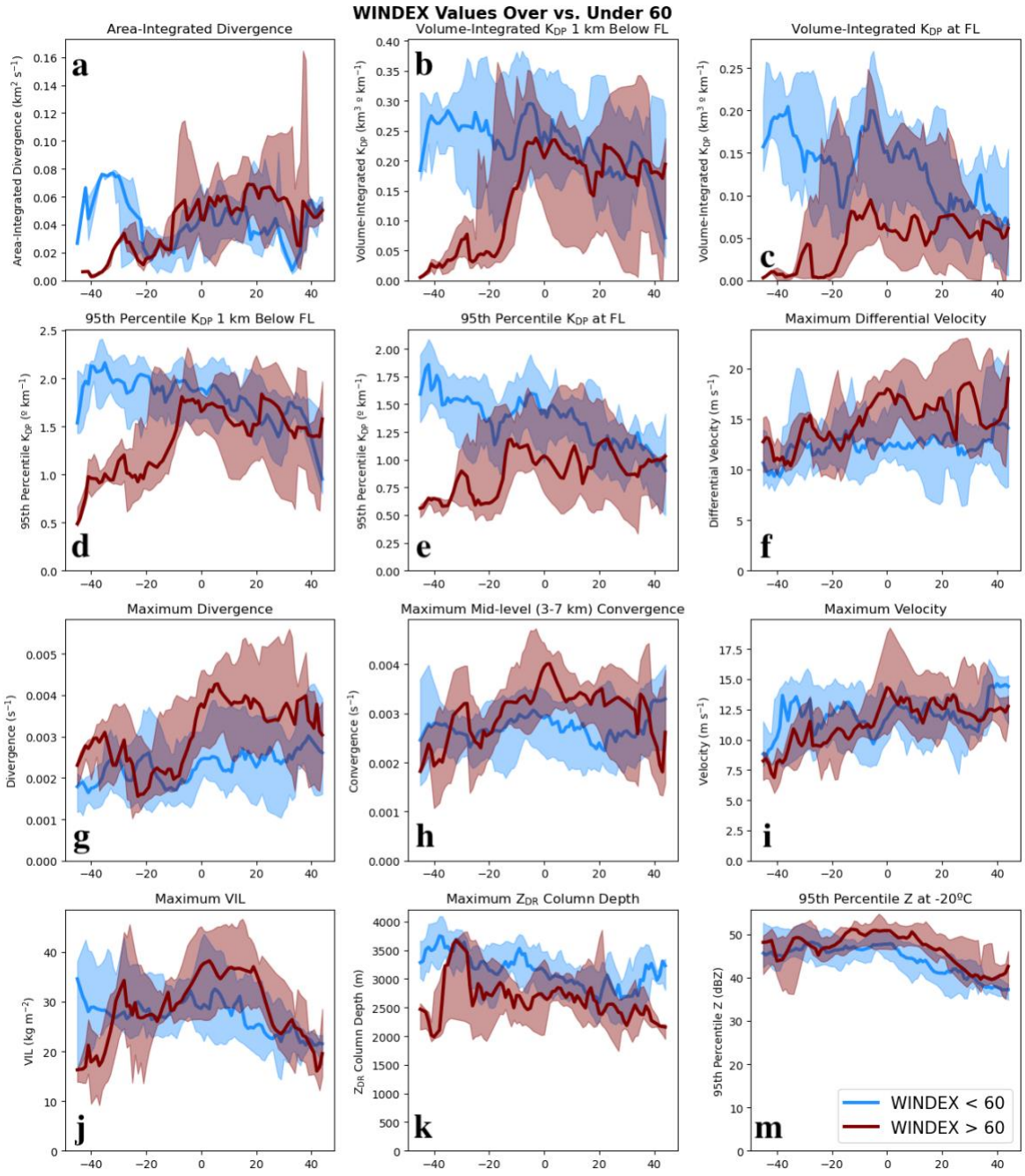

Figure 23. DS-relative 25th percentile, median, and 75th percentile time series plots of cases with WINDEX values over 60 (red line, shaded) and under 60 (blue line, shaded).

DS time. Overall, the medians values of all divergence- and velocity-related variables for O60 cases are greater than those of the U60 cases, suggesting that higher WINDEX and LR values may lead to stronger downdrafts reaching near the surface (as in Srivastava 1985; 1987).

The last few variables include the maximum Z_{DR} column depth, maximum VIL, and 95th percentile Z at -20 ºC. For maximum Z_{DR} column depth (Figure 23k), U60 is greater than O60 throughout the entire time window, suggesting that lower WINDEX values are associated with higher Z_{DR} column depths. This result is unexpected at first, but it is possible that the maximum height of the Z_{DR} columns in some stronger cases are being limited by giant hail near the top of the updraft dominating the Z signal, preventing them from growing as tall. All cases generally decrease over time as well, and in both conditions, values become closer together after the DS time. Lastly, maximum VIL (Figure 23j) and 95th percentile Z at -20 ºC (Figure 23m) depict similar information wherein precipitation maximizes at or near mid-levels around the DS time then begins to decrease afterwards. For 95th percentile Z at -20 ºC, the median values of the O60 cases are slightly larger than those of the U60 cases. For maximum VIL (Figure 23j), U60 has a small peak near the DS time, whereas O60 has a large peak just after the DS time, roughly 8 kg m^{-2} higher than U60 cases. This discrepancy may again be due to environmental moisture being considered in the WINDEX calculation, so higher low-level moisture and lower mid-level moisture values would increase WINDEX values, and more available moisture could increase VIL values as well.

Some notable differences between the WINDEX and 0–2-km LR plots are seen in maximum low-level divergence (Figures 23g and 24g), mid-level convergence (Figures 23h and 24h), and VIL (Figures 23j and 24j). In all of these plots, the separation between the O60 and U60 cases (O60 is greater than U60 in all plots) is larger than that between the O8 and U8 cases. However, variables do still peak at nearly the same time in both conditions. Overall, the median values that are most similar for these environmental conditions include area-integrated divergence and maximum velocity. Variables with median values of U60 greater than O60

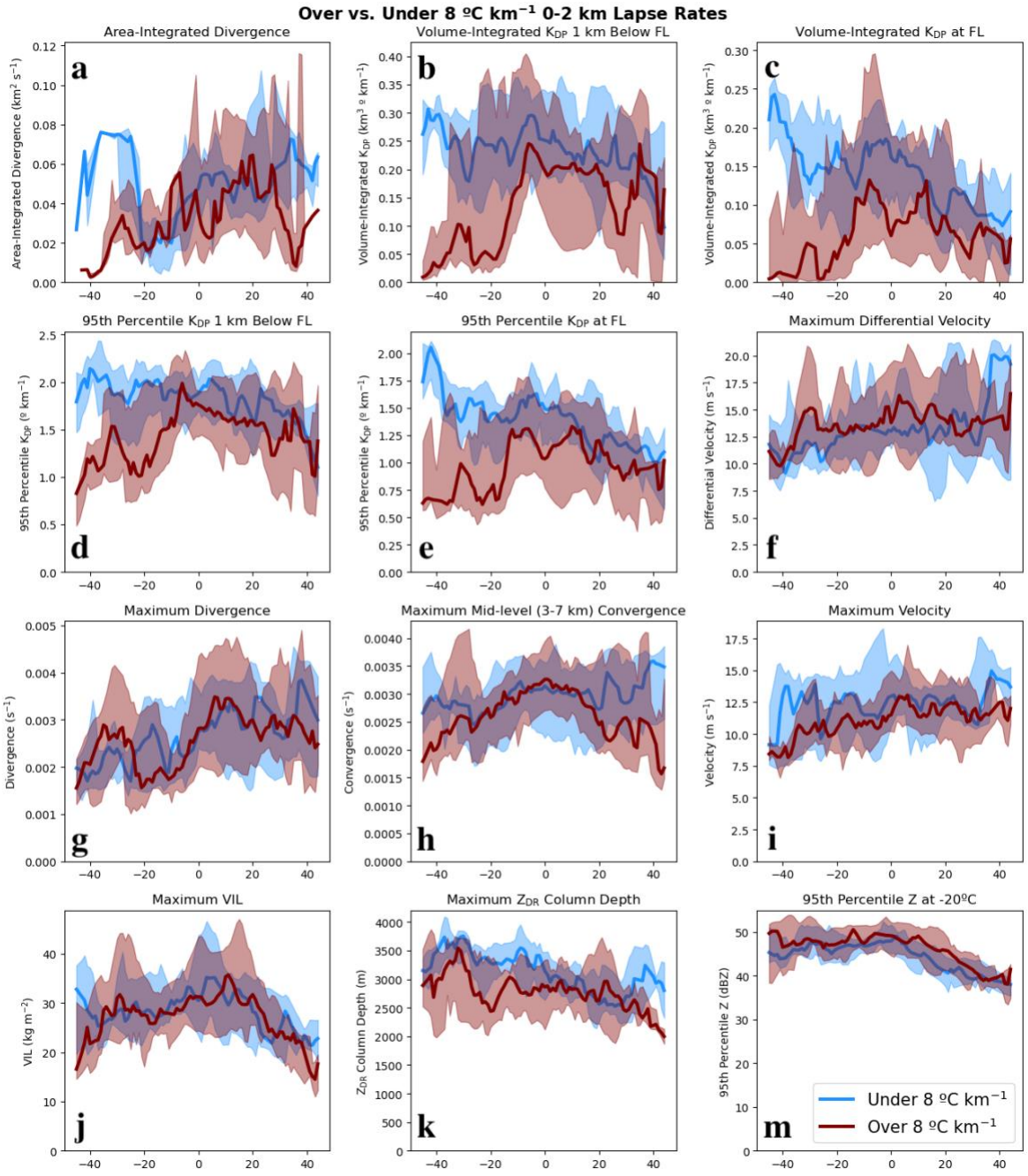

Figure 24. DS-relative 25th percentile, median, and 75th percentile time series plots of cases with 0 to 2 km LR over 8 ºC km^{-1} (red line, shaded) and under 8 ºC km^{-1} (blue line, shaded).

include volume-integrated and 95th percentile K_{DP} at and 1-km below the freezing level and maximum Z_{DR} column depth. Variables with median values of O60 greater than U60 include maximum differential velocity and 95th percentile Z at -20 ºC, maximum low-level divergence, mid-level convergence, and VIL.

3.4 Case study of 2023 August 11 Wichita Falls, TX downburst

During the afternoon and early evening of 10 August 2023, surface temperatures exceeded 40 ºC over a wide swath of southwest Oklahoma and northern Texas due to strong radiative heating and southerly winds only reaching about 10 m s^{-1}. The nearby upper-air sounding from FWD at 00 UTC 11 August 2023 (Figure 25a) indicated that the convective temperature in the area was near 43ºC and the low-level LR was dry adiabatic (9.8 K km^{-1}) up to

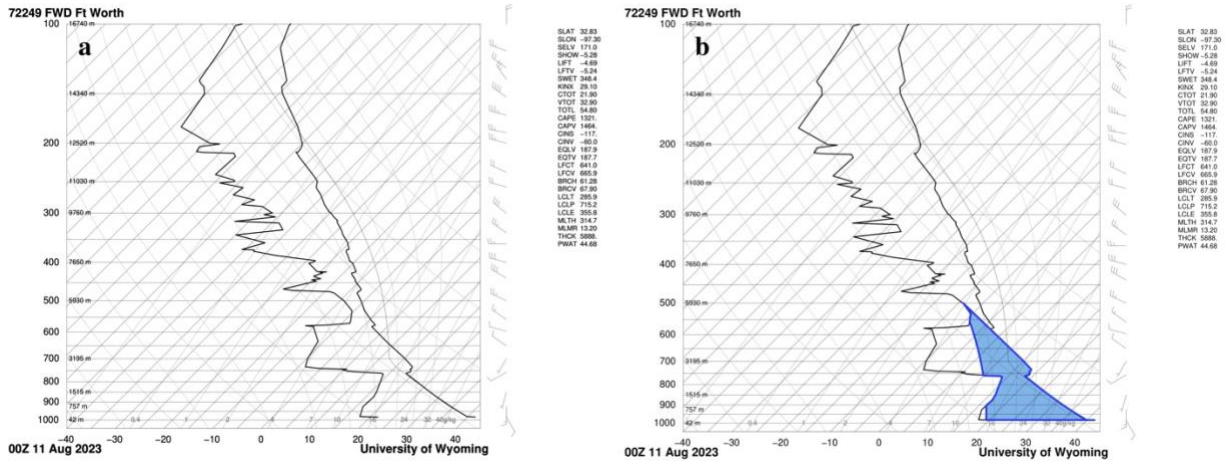

Figure 25. a) 11 August 2023 00 UTC radiosonde sounding from FWD obtained from the University of Wyoming sounding archive and b) the same radiosonde sounding with DCAPE shown (blue shaded area).

nearly 4 km AGL, which is relatively steep for mid-levels, and indicates a favorable environment for downbursts to occur (Srivastava 1985). The surface-based Convective Available Potential Energy (CAPE) was 1321 J kg^{-1}, and Figure 25b shows a large area of negative buoyancy (e.g., Downdraft CAPE) with a large "inverted V" profile. This sounding is characteristic of August in the southern Great Plains, an area and time of year that frequently experiences extreme downburst events (Romanic et al. 2022). In all, this was a classic setup for strong to severe air-mass thunderstorms, including downbursts.

By 2100 UTC, some locations had reached the convective temperature and storms initiated in TX just west of Abilene. Over the following 4 hours, single- and multi-cell convection filled in over north-central TX from north of San Angelo to west of Fort Worth,

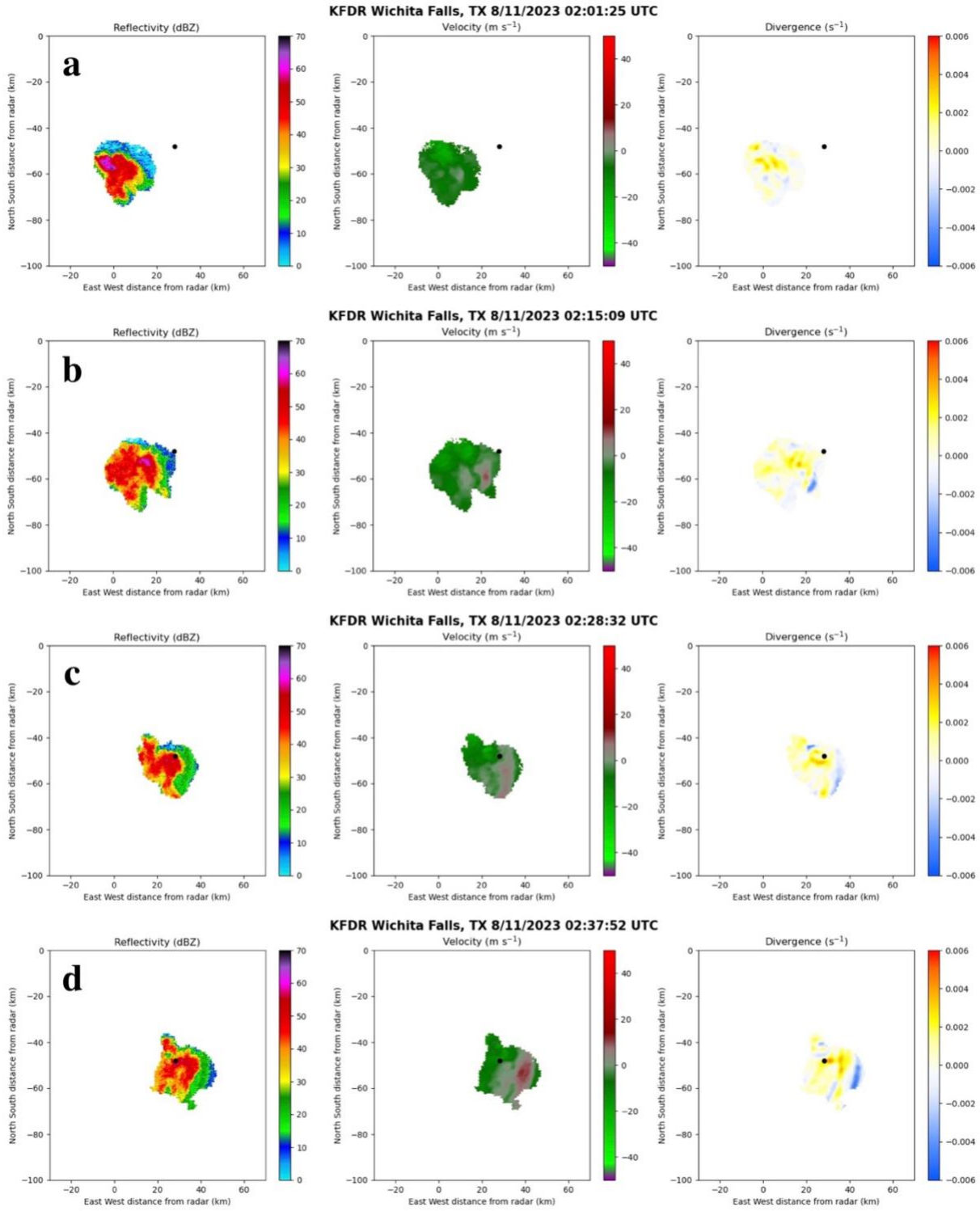

Figure 26. From left to right, Z (dBZ), velocity (ms^{-1}), and divergence (s^{-1}) for the MCIT-identified downburst-producing cell on 11 August 2023 Wichita Falls, TX downburst event at a) 02:01 UTC, b) 02:15 UTC, c) 02:28 UTC, and d) 02:37 UTC. The black dot shows the location of the storm report made at 02:30 UTC.

producing numerous outflow boundaries across the region as storms collapsed. At 01:23 UTC,

outflow boundaries from two storms near Munday and Olney, TX collided north of Seymour, TX

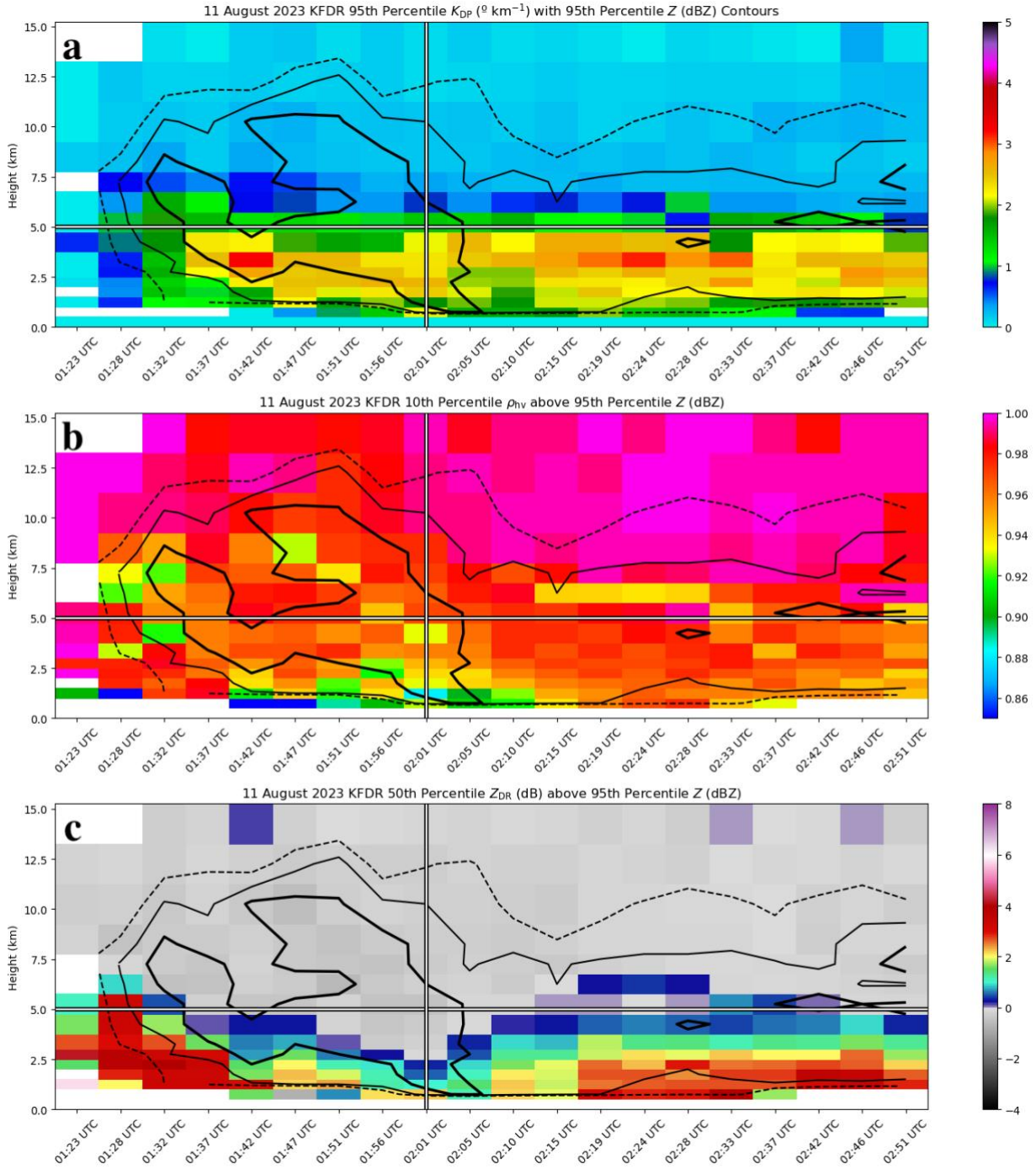

Figure 27. Time–height plots from KFDR on 11 August 2023 of a) 95th percentile K_{DP}, b) 10th percentile ρ_{hv} above 95th percentile Z, and c) median Z_{DR} above 95th percentile Z, all with 95th percentile Z contours overlayed (dashed line is 50 dBZ, thin solid line is 55 dBZ, and thick solid line is 60 dBZ). The white horizontal line marks the approximate freezing level, and the white vertical line marks the DS time in all plots.

and the first radar echoes of the Wichita Falls cell appeared. This storm continued to intensify

over the next 40 minutes until it produced its first DS near 02:01 UTC (Figure 26a) to the west-southwest of Wichita Falls. This DS continued to strengthen (Figure 26b) and passed over the storm report location at 02:28 UTC (Figure 26c), then persisted until the storm began to weaken around 02:37 UTC (Figure 26d). At its strongest, this downburst knocked down power poles, uprooted large trees, collapsed a 500-ft tall radio tower, caused significant damage to a strip mall and apartment building, and overturned a semi-truck on Interstate 44. The Wichita Falls Mesonet station reported a gust of 61 mph and radar estimated wind speeds of 60 to 70 mph aloft, though these were deemed to be underestimated as damage consistent with 90 to 100 mph winds was observed (NWS Norman).

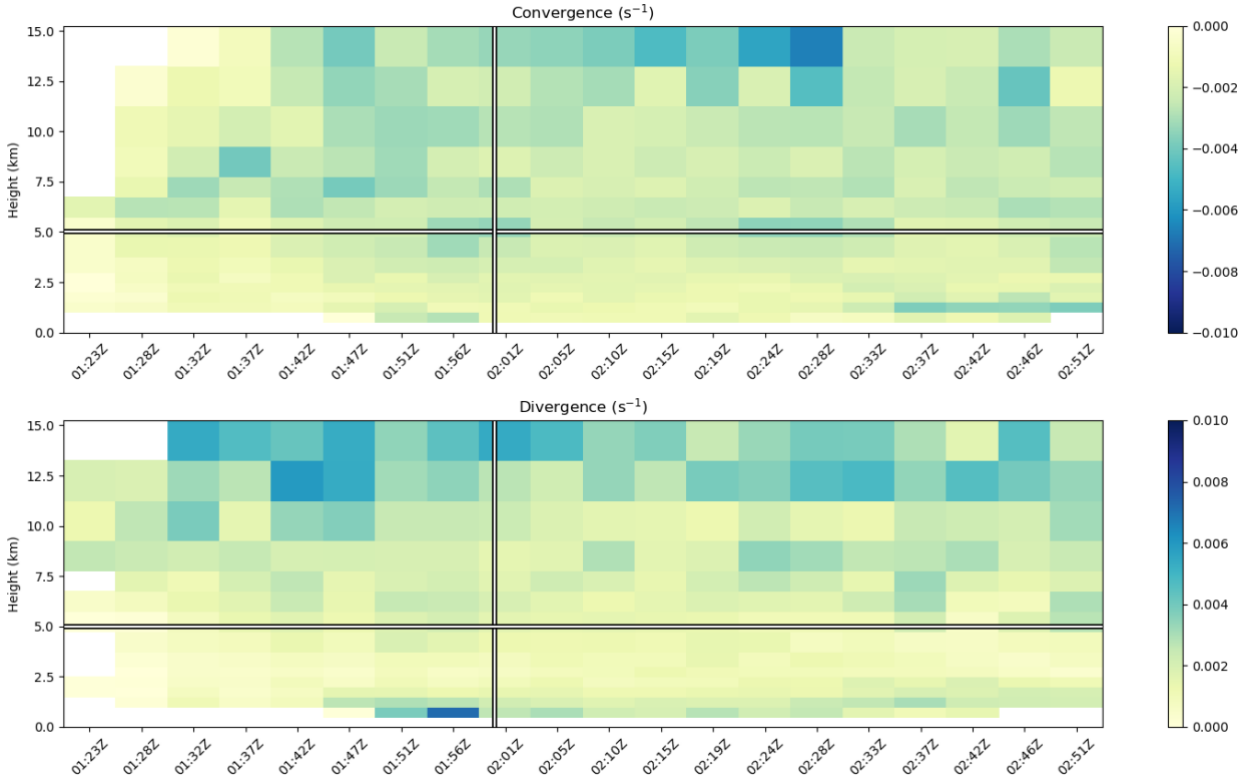

Figure 28. Time–height plots from KFDR on 11 August 2023 of a) 90th percentile convergence and b) 90th percentile divergence. The white horizontal line marks the approximate freezing level, and the white vertical line marks the DS time in all plots.

Since this was an isolated single-cell storm that produced strong downburst wind damage and was only about 56 km from the nearest WSR–88D radar (KFDR), the variables of interest

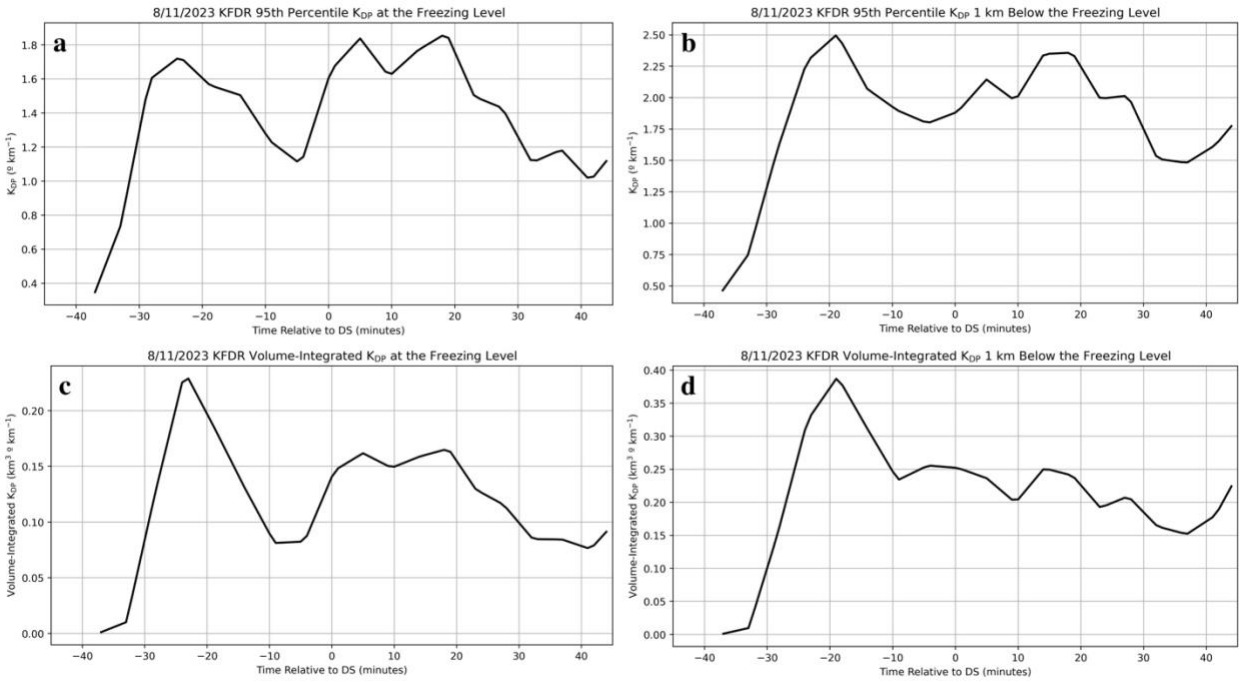

Figure 29. DS-relative time series of 95th percentile K_{DP} a) at the freezing level and b) 1-km below the freezing level, and volume-integrated K_{DP} c) at the freezing level and d) 1-km below the freezing level.

discussed in the previous sections are investigated to see which, if any, downburst signatures or features appeared. A time–height plot of K_{DP} (Figure 27a) shows a K_{DP} core appeared at 1:37 UTC and rapidly intensified to over 3.5 ° km^{-1} before beginning to descend at 01:51 UTC until the time of the DS. Similarly, the contours of Z (Figure 27a) show a Z core with values over 60 dBZ beginning to rapidly descend from 10 km AGL at 01:51 UTC which eventually reach the surface at and immediately after the DS time. Another Z core with similar values appears to descend from near 8 km AGL at 01:32 UTC, before the main descending core associated with this downburst event, which is just before the initial appearance of the K_{DP} core. This is likely cycling occurring within the storm, but it is also possible that the descent of the initial Z core cooled the air as hydrometeors began to melt and enhanced the descent of the main Z core. Next, though there is a negative Z_{DR} bias in the data, a strong Z_{DR} trough is apparent beginning at 01:51 UTC (Figure 27c) and lasting through 02:15 UTC with a collocated ρ_{hv} drop (Figure 27b) at the same time. Lastly, there is a slight increase in convergence (Figure 28a) at the freezing level (i.e.,

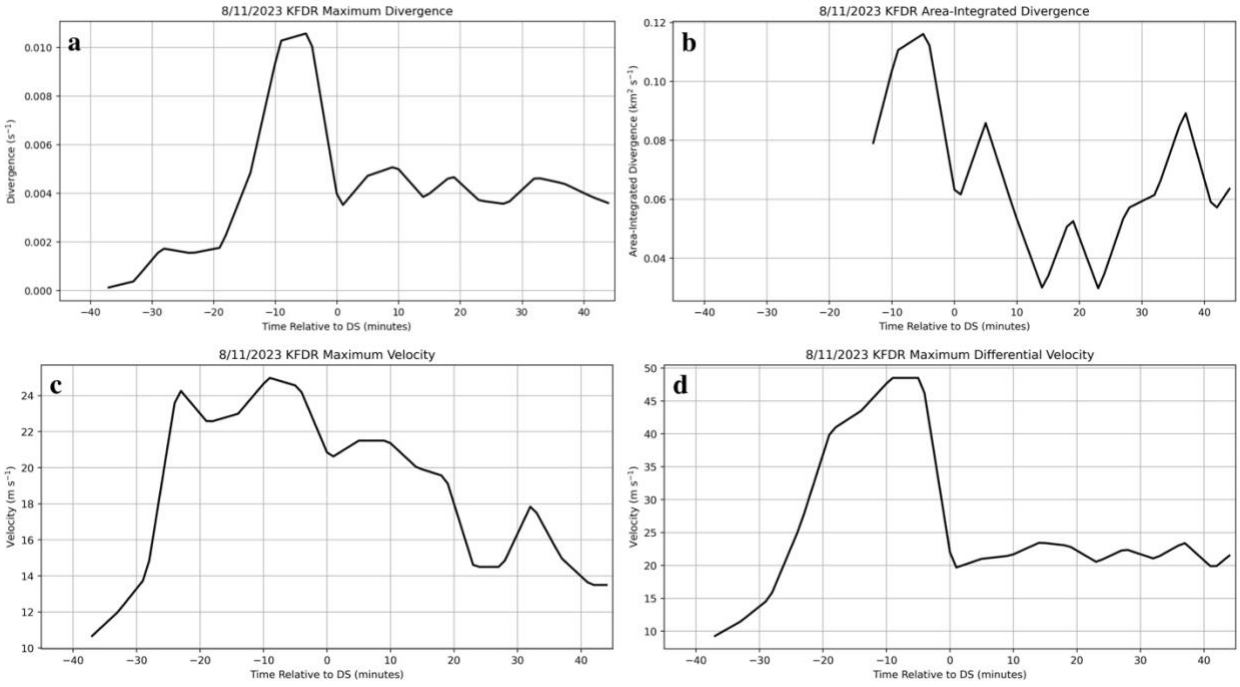

Figure 30. DS-relative time series of a) maximum divergence, b) area-integrated divergence, c) maximum velocity, and d) maximum differential velocity.

mid-levels) with stronger convergence values above 7 km AGL, and a strong increase in surface divergence (Figure 28b) exceeding 0.008 s^{-1} in the volume scan before DS time, when the downdraft first reached the surface. All of these signals occur in the 20 minutes leading up to the DS time, making them quite prominent signatures.

The first analyzed time series plots are the 95th percentile and volume-integrated K_{DP}. All plots tell a similar story, but the volume-integrated K_{DP} plots give insight into how large this storm was as well as the K_{DP} values within it. In the 95th percentile K_{DP} plots at (Figure 29a) and 1 km below (Figure 29b) the freezing level, K_{DP} values increase rapidly after storm initiation. At the freezing level, K_{DP} values peak nearly 25 minutes before the DS time, and as the K_{DP} core descends, K_{DP} values 1 km below the freezing level peak 5 minutes later, 20 minutes before the DS time. The K_{DP} core continues to descend and both plots show a minimum in K_{DP} values 5 minutes before the DS time, similar to Figure 27a. Volume-integrated K_{DP} at (Figure 29c) and 1-km below (Figure 29d) the freezing level show the same signals, peaking and reaching minimum

at the same times, but show a more pronounced signal since this storm was so large (roughly 30

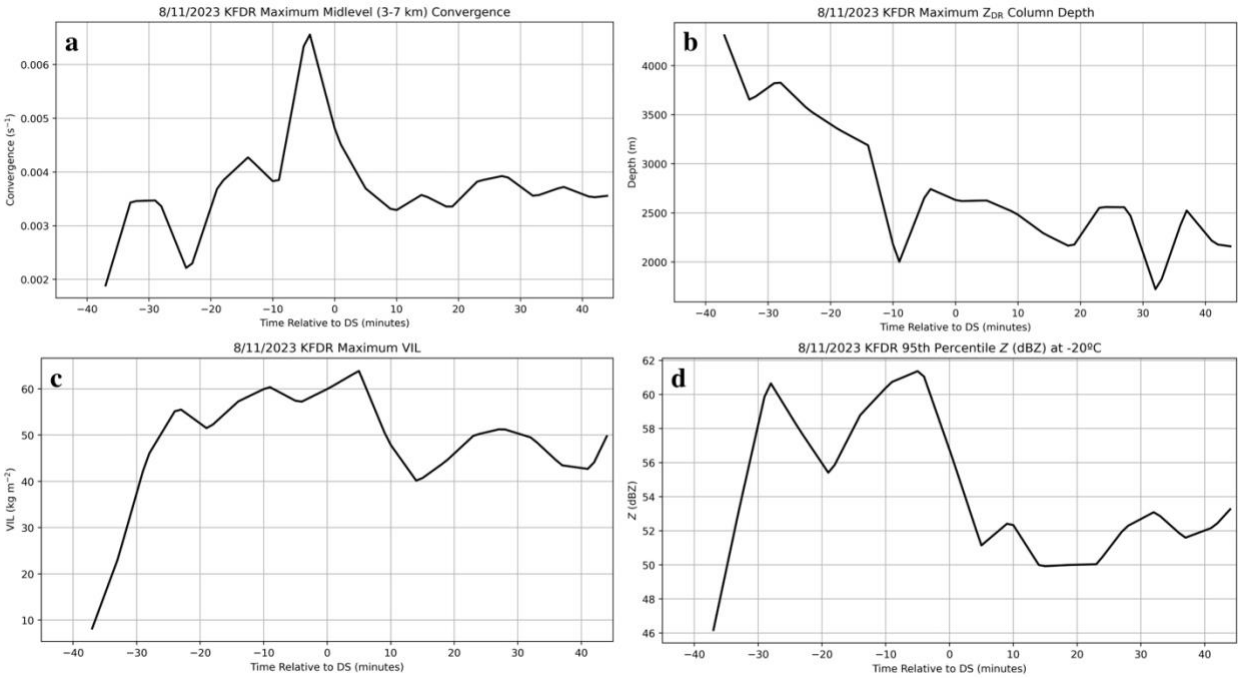

Figure 31. DS-relative time series of a) maximum mid-level convergence, b) maximum Z_{DR} column depth, c) maximum VIL, and d) 95th percentile Z at -20 ºC.

km across at its largest). The extremely rapid increase in these plots beginning about 30 minutes before the DS time then rapid decrease just 10 minutes later compliment Figure 27a, depicting a descending K_{DP} core. Since these signals all occurred within the time window leading up to the DS time, they have the potential to serve as precursors to strong downburst occurrence given the known favorable environment.

Next, the maximum divergence (Figure 30a), area-integrated divergence (Figure 30b), maximum velocity (Figure 30c), and maximum differential velocity (Figure 30d) are investigated. All four plots show a large peak within 10 minutes of the DS time, which aligns with Figure 28b where low-level divergence spikes just before the DS time. Surprisingly, maximum divergence reaches 0.01 s^{-1}, area-integrated divergence reaches just under 0.12 s^{-1}, maximum velocity reaches nearly 25 m s^{-1}, and maximum differential velocity reaches about 48 m s^{-1}, far surpassing all thresholds used in Table 1.

The plots of maximum mid-level convergence (Figure 31a), VIL (Figure 31b), Z_{DR} column depth (Figure 31c), and 95th percentile Z at -20 ºC (Figure 31d) are explored last and they show signals as well. The maximum midlevel convergence plot gradually increases until it peaks 5 minutes before the DS time at over 0.006 s^{-1}, then rapidly decreases over the next 10 minutes, coincident with the peaks in maximum velocity and differential velocity after the DS time. This makes sense as midlevel convergence would be expected to maximize prior to low-level velocity maximizing as the downdraft descends. Maximum VIL peaks immediately after the DS time, likely associated with large amounts of precipitation collapsing through the layer with the storm. The maximum Z_{DR} column height gradually decreases over the time window, but there is a large decrease nearly 10 minutes before the DS time wherein the storm began to collapse which could be due to large hailstones aloft beginning to fall and "shortening" the column depth by lowering Z_{DR} values near the top. The 95th percentile Z at -20 ºC peaks 5 minutes before the DS time, as seen in Figure 27a, then rapidly decreases through the DS time. Overall, this was a remarkable case which displayed strong signatures in the variables considered and aptly demonstrates the utility and lifecycle of the previously discussed potential polarimetric downburst precursor signature.

Chapter 4

Conclusions and Future Work

4.1 Summary and conclusions

Single-polarization, polarimetric, and derived radar variables along with commonly observed features and environmental conditions for 41 downburst cases were investigated to determine which produced the most prominent signatures and/or precursors by automatically identifying and tracking downburst-producing storms throughout their lifecycle. This was accomplished with the MCIT algorithm (Hu et al. 2019), which uses VIL (Greene and Clark 1972) and the Meyer watershed algorithm (1994) to identify and track all storm cells in the domain of WSR–88D radars and assign them each a storm ID (SID). Upon finding the SID of the downburst-producing storm cell of interest for each case, Z, radial velocity, Z_{DR}, ρ_{hv}, K_{DP}, VIL, divergence, convergence, and Z_{DR} column depth were gathered or calculated, then extracted at every radar gate within the MCIT-identified cell boundary and interpolated to a common height grid of 50 m with Py-ART (Helmus and Collis 2016) for comparing across different heights. WINDEX and 0–2-km LR values at the nearest radar for each case were calculated as well from Rapid Refresh model data (Benjamin et al. 2016).

Features including a descending Z core (DRC), a K_{DP} core near or below the freezing level or a descending K_{DP} core, a Z_{DR} trough extending below the freezing level with a collocated ρ_{hv} drop, divergence at the 0.5º tilt, and mid-level (3–7 km) convergence were determined to be present or not for each individual case by constructing time–height plots throughout the storm's

lifecycle and only considering the 30 minutes leading up to and 10 minutes after the storm report (SR) time. Percentiles of these variables were used in an effort to isolate the most intense part of the storm for analysis, including 95th percentile Z and K_{DP}, median Z_{DR} and 10th percentile ρ_{hv} above the 95th percentile Z, and 90th percentile low-level divergence and mid-level convergence. In all, 88% of cases contained a DRC that often appeared within one volume scan of the SR time, and 95% contained a present and/or descending K_{DP} core that typically appeared within 5 to 10 minutes of the SR time, but also appeared 15 to 30 minutes prior to the SR time in a quarter of cases, agreeing with the findings of Kuster et al. (2021). A Z_{DR} trough was present in 98% of cases with a collocated ρ_{hv} drop in 88% of cases within 10 minutes of the SR time for most cases, though they appeared more than 20 minutes before the SR time in 8 cases (5 in the Southwest U.S. and 3 in the Northeast U.S.). The magnitude of low-level divergence and mid-level convergence reached the chosen threshold of 0.0025 s^{-1} (Dance and Potts 2002; Wilson et al. 1984) in 85% and 76% of cases, respectively. This is somewhat lower than expected, but could be due to the chosen threshold, low-level divergence occurring below the radar beam at the lowest elevation angle, and/or the storm of interest occurring farther from the nearest radar and losing resolution due to beam broadening.

Raw variable and/or signature time series were composited for each case and looked at in sum or split by geographic region or environmental favorability, characterized by either WINDEX or the 0–2-km LR. These composites were done with respect to the time of the storm report (SR), the appearance of a divergence signature (DS), or maximum VIL (MV) for each case to see if consistent trends emerged across cases relative to downburst occurrence. These signals were initially quite hard to identify in the composite plots of raw values due to dramatic differences in storm intensity and size between cases. When normalized by the maximum value

of each time series, however, the evolution of each signature became clearer. Ultimately, the DS time became the main anchor time of subsequent analysis because it removed any uncertainty associated with using SR time (Trapp et al. 2006) and displayed the clearest signals leading up to and after downburst occurrence. At or near the surface, maximum and area-integrated divergence and maximum velocity and differential velocity had the most prominent signals, which occurred at or just following the DS time. Aloft, the 95th percentile and volume-integrated K_{DP} at and 1-km below the freezing level, maximum mid-level convergence, and VIL most clearly showed precursor signatures before the downburst reached the surface. On average, K_{DP} at the freezing level peaked 10 minutes before, K_{DP} 1-km below the freezing level peaked 5 minutes before, and mid-level convergence and VIL began increasing 20 minutes before the DS time). Variables that displayed no or a less prominent signal were maximum Z_{DR} column depth and 95th percentile Z at -20 ºC.

The final part of the analysis involved investigating all variables based on region (eastern U.S. versus western U.S.) and environmental conditions (WINDEX and 0–2-km LR). When cases were separated based on region, the main takeaway was that higher K_{DP} and lower divergence, velocity, VIL, and Z_{DR} column depth values were most common in eastern cases, while higher divergence, velocity, VIL, and Z_{DR} column depth and lower K_{DP} values were more common in western cases. Also of note, western cases had more favorable environments than eastern cases, with 0–2-km LR reaching or exceeding 8 º km^{-1} and WINDEX values reaching or exceeding 60 more often. One possible explanation for the observed differences in radar signatures between regions is that less precipitation loading may be needed to initiate downbursts due to the typically more favorable thermodynamic environments in the western U.S., as hypothesized in Kuster et al. (2021), thus leading to lower K_{DP} values but stronger downburst

signatures in the wind fields. Another possible explanation, and one that is mutually compatible with the first, is that eastern storms produce smaller hail on average (Allen and Tippett 2015), which can accumulate and form oblate surface meltwater tori when melting near and below the freezing level, thereby increasing K_{DP} values (Kumjian et al. 2019). In contrast, western U.S. storms with potentially larger average hail sizes may produce higher Z and VIL values but ultimately lower K_{DP} when undergoing melting. Mid-level convergence was also much less frequently observed in the Southeast compared to the Midwest and Southwest as well, similar to results found by Isaminger (1988).

Splitting cases by WINDEX values and 0–2-km LR produced exceeding similar results. Environments with values of WINDEX above 60 and 0–2-km LR above 8 ºC km^{-1} typically had higher values of differential velocity, low-level divergence, mid-level convergence, VIL, and 95th percentile Z at -20 ºC, while environments with WINDEX below 60 and 0–2-km LR below 8 ºC km^{-1} typically had higher values of K_{DP} and Z_{DR} column height. These results for both conditions are nearly the same as the results for the regional comparison since western cases experienced WINDEX above 60 and 0–2-km LR above 8 ºC km^{-1} (i.e., a more favorable environment) most often, while eastern cases experienced WINDEX and 0–2-km LR values below 60 and 8 º km^{-1} (i.e., less favorable environment), respectively most often. It is worth briefly mentioning that based on these results, any downburst detection algorithm that relies on thresholds may need to vary them with the region and/or thermodynamic environment.

There are important caveats to this study that should be mentioned as well. The most important one is the fact that null, non-downburst-producing cases were not explored for comparison against the downburst-producing cases that were the emphasis of this study. Because of this, the observed signatures and potential precursors possibly associated with downburst

occurrence may also be present in storms that do not produce downbursts. Also, the downburst-producing cases in this study may not reach the thresholds used because they were not differentiated based on strength. Lastly, although this study did expand on prior research by automating storm identification and tracking to investigate 41 total cases, this is still a rather limited dataset. This is especially apparent when separating the cases by region (Figure 2) given there are 19 Southwest and 12 Southeast cases, but only 6 Midwest, 4 Northeast, and 0 Northwest cases, although this mirrors the climatology of favorable downburst environments presented in Romanic et al. (2022).

4.2 Future work

Based on some of the caveats described above, future work should analyze null, non-downburst producing cases which occurred in similar environments alongside the downburst-producing cases analyzed here. This would more confidently assess whether certain signatures or potential precursors and/or thresholds can be used to accurately discriminate downburst features from features of non-downburst storms. Another endeavor should be increasing the dataset size and analyzing downburst- and non-downburst-producing storms in all regions of the U.S. in an effort to create more robust statistics. The use of polarimetric phased-array radar should also be explored for downburst detection to evaluate what enhanced temporal update times and/or mid-level scanning coverage may offer forecasters as they identify downburst precursor signatures.

Reference List

Adachi, T., K. Kusunoki, S. Yoshida, K. Arai, and T. Ushio, 2016: High-speed volumetric observation of a wet microburst using X-band phased array weather radar in Japan. *Mon. Wea. Rev.*, **144**, 3749–3765, https://doi.org/10.1175/MWR-D-16-0125.1.

Allen, J. T., and M. K. Tippett, 2015: The characteristics of United States hail reports: 1955–2014. *Electronic J. Severe Storms Meteor.*, **10 (3)**, 1–31, https://doi.org/10.55599/ejssm.v10i3.60.

Atkins, N. T., and R. M. Wakimoto, 1991: Wet microburst activity over the southeastern United States: implications for forecasting. *Wea. Forecasting*, **6**, 470–482, https://doi.org/10.1175/1520-0434(1991)006<0470:WMAOTS>2.0.CO;2.

Atlas, D., C. W. Ulbrich, and C. R. Williams, 2004: Physical origin of a wet microburst: observations and theory. *J. Atmos. Sci.*, **61**, 1186–1195, https://doi.org/10.1175/1520-0469(2004)061<1186:POOAWM>2.0.CO;2.

Benjamin, S. G., and Coauthors, 2016: A North American hourly assimilation and model forecast cycle: the Rapid Refresh. *Mon. Wea. Rev.*, **144**, 1669–1694, https://doi.org/10.1175/MWR-D-15-0242.1.

Carlin, J. T., A. V. Ryzhkov, J. C. Snyder, and A. Khain, 2016: Hydrometeor mixing ratio retrievals for storm-scale radar data assimilation: utility of current relations and potential benefits of polarimetry. *Mon. Wea. Rev.*, **144**, 2981–3001, https://doi.org/10.1175/MWR-D-15-0423.1.

Dance, S., and R. Potts, 2002: Microburst detection using agent networks. *J. Atmos. Oceanic Technol.*, **19**, 646–653, https://doi.org/10.1175/1520-0426(2002)019<0646:MDUAN>2.0.CO;2.

Dodge, J., J. Arnold, G. Wilson, J. Evans, T. T., Fujita, 1986: The Cooperative Huntsville Meteorological Experiment (COHMEX). *Bull. Amer. Meteor. Soc.*, **67 (4)**, 417–419.

Dotzek, N., and K. Friedrich, 2009: Downburst-producing thunderstorms in southern Germany: radar analysis and predictability. *Atmos. Res.*, **93**, 457–473, https://doi.org/10.1016/j.atmosres.2008.09.034.

Emanuel, K. A., 1994: *Atmospheric Convection*. Oxford University Press, New York, 172 pp.

Frugis, B. J., 2018: Using specific differential phase to predict significant severe thunderstorm wind damage across the northeastern United States. *29th Conference on Severe Local Storms*, Stowe, VT, American Meteorological Society, 21, https://ams.confex.com/ams/29SLS/meetingapp.cgi/Paper/348206.

Fujita, T. T., 1978: Manual of downburst identification for Project NIMROD. SMRP Research Paper 156, University of Chicago, 104 pp. [NTIS PB-286048.]

———, T. T., 1981: Tornadoes and downbursts in the context of generalized planetary scales. *J. Atmos. Sci.*, **38**, 1511–1534, https://doi.org/10.1175/1520-0469(1981)038<1511:TADITC>2.0.CO;2.

———, T. T., 1985: The downburst: microburst and macroburst. SMRP Research Paper 210, University of Chicago, 122 pp. [NTIS PB85-148880.]

———, T. T., and F. Caracena, 1977: An analysis of three weather-related aircraft accidents. *Bull. Amer. Meteor. Soc.*, **58 (11)**, 1164–1181, https://doi.org/10.1175/1520-0477(1977)058<1164:AAOTWR>2.0.CO;2.

———, T. T., and H. R. Byers, 1977: Spearhead echo and downburst in the crash of an airliner. *Mon. Wea. Rev.*, **105 (2)**, 129–146, https://doi.org/10.1175/1520-0493(1977)105<0129:SEADIT>2.0.CO;2.

Greene, D. R., and R. A. Clark, 1972: Vertically integrated liquid water—a new analysis tool. *Mon. Wea. Rev.*, **100**, 548–552.

Heinselman, P. L., D. L. Priegnitz, K. L. Manross, T. M. Smith, and R. W. Adams, 2008: Rapid sampling of severe storms by the National Weather Radar Testbed phased array radar. *Wea. Forecasting*, **23**, 808–824, https://doi.org/10.1175/2008WAF2007071.1.

Helmus, J.J. and S.M. Collis, 2016: The Python ARM Radar Toolkit (Py-ART), a library for working with weather radar data in the python programming language. *J. Open Res. Softw.*, **4 (1)**, 25, http://doi.org/10.5334/jors.119.

Hjelmfelt, M. R., R. D. Roberts, H. D. Orville, J. P. Chen, and F. J. Kopp, 1989: Observational and numerical study of a microburst line-producing storm. *J. Atmos. Sci.*, **46 (17)**, 2731–2744, https://doi.org/10.1175/1520-0469(1989)046<2731:OANSOA>2.0.CO;2.

Hu, J., D. Rosenfeld, D. Zrnic, E. Williams, P. Zhang, J. C. Snyder, A. Ryzhkov, E. Hashimshoni, R. Zhang, and R. Weitz, 2019: Tracking and characterization of convective cells through their maturation into stratiform storm elements using polarimetric radar and lightning detection. *Atmos. Res.*, **226**, 192–207, https://doi.org/10.1016/j.atmosres.2019.04.015.

Isaminger, M. A., 1988: A preliminary study of precursors to Huntsville microbursts. Lincoln Laboratory Project Rep. ATC-153, 22 pp.

James, R. P., and P. M. Markowski, 2010: A numerical investigation of the effects of dry air aloft on deep convection. *Mon. Wea. Rev.*, **138**, 140–161, https://doi.org/10.1175/2009MWR3018.1.

Kitzmiller, D. H., W. E. McGovern, and R. E. Saffle, 1995: The WSR-88D severe weather potential algorithm. *Wea. Forecasting*, **10**, 141–159, https://doi.org/10.1175/1520-0434(1995)010<0141:TWSWPA>2.0.CO;2.

Knupp, K. R., 1989: numerical simulation of low-level downdraft initiation within precipitating cumulonimbi: some preliminary results. *Mon. Wea. Rev.*, **117**, 1517–1529, https://doi.org/10.1175/1520-0493(1989)117<1517:NSOLLD>2.0.CO;2.

Kumjian, M. R., Z. J. Lebo, and A. M. Ward, 2019: Storms producing large accumulations of small hail. *J. Appl. Meteor. Climatol.*, **58**, 341–364, https://doi.org/10.1175/JAMC-D-18-0073.1.

Kuster, C. M., P. L. Heinselman, and T. J. Schuur, 2016: Rapid-update radar observations of downbursts occurring within an intense multicell thunderstorm on 14 June 2011. *Wea. Forecasting*, **31**, 827–851, https://doi.org/10.1175/WAF-D-15-0081.1.

———, C. M., B. R. Bowers, J. T. Carlin, T. J. Schuur, J. W. Brogden, R. Toomey, and A. Dean, 2021: Using K_{DP} cores as a downburst precursor signature. *Wea. Forecasting*, **36**, 1183–1198, https://doi.org/10.1175/WAF-D-21-0005.1.

Lakshmanan, V., T. Smith, G. Stumpf, and K. Hondl, 2007: The Warning Decision Support System–Integrated Information. *Wea. Forecasting*, **22**, 596–612, https://doi.org/10.1175/WAF1009.1.

Mahale, V. N., G. Zhang, and M. Xue, 2016: Characterization of the 14 June 2011 Norman, Oklahoma, downburst through dual-polarization radar observations and hydrometeor classification. *J. Appl. Meteor. Climatol.*, **55**, 2635–2655, https://doi.org/10.1175/JAMC-D-16-0062.1.

Markowski, P. M., and Y. P. Richardson, 2010: *Mesoscale Meteorology in Midlatitudes*. Wiley-Blackwell, 27 pp.

McCarthy, J., J. W. Wilson, and T. T. Fujita, 1982: The joint airport weather studies project. *Bull. Amer. Meteor. Soc.*, **63 (1)**, 15–22, https://doi.org/10.1175/1520-0477(1982)063<0015:TJAWSP>2.0.CO;2.

———, J., and J. W. Wilson, 1985: The Classify, Locate, and Avoid Wind Shear (CLAWS) project at Denver's Stapleton International Airport: operational testing of terminal weather hazard warnings with an emphasis on microburst wind shear. *2nd International Conference on the Aviation Weather System*, Montreal, Canada, American Meteorological Society, 247–256.

Meyer, F., 1994: Topographic distance and watershed lines. *Signal Process*., **38 (1)**, 113–125, https://doi.org/10.1016/0165-1684(94)90060-4.

NWS, 2011: Weather spotter's field guide. NOAA, Accessed 10 November 2023, https://www.weather.gov/spotterguide/downbursts.

Proctor, F. H., 1989: Numerical simulations of an isolated microburst. Part II: sensitivity experiments. *J. Atmos. Sci.*, **46 (14)**, 2143–2165, https://doi.org/10.1175/1520-0469(1989)046<2143:NSOAIM>2.0.CO;2.

Pryor, K. L., 2015: Progress and developments of downburst prediction applications of GOES. *Wea. Forecasting*, **30**, 1182–1200, https://doi.org/10.1175/WAF-D-14-00106.1.

Richter, H., J. Peter, and S. Collis, 2014: Analysis of a destructive wind storm on 16 November 2008 in Brisbane, Australia. *Mon. Wea. Rev.*, **142**, 3038–3060, https://doi.org/10.1175/MWR-D-13-00405.1.

Rinehart, R. E., 2010: *Radar for Meteorologists*. 5th Edition, Rinehart Publications, Missouri.

Roberts, R. D., and J. W. Wilson, 1989: A proposed microburst nowcasting procedure using single-doppler radar. *J. Appl. Meteor. Climatol.*, **28**, 285–303, https://doi.org/10.1175/1520-0450(1989)028<0285:APMNPU>2.0.CO;2.

Romanic, D., M. Taszarek, and H. Brooks, 2022: Convective environments leading to microburst, macroburst and downburst events across the United States. *Wea. Clim. Extremes*, **37**, https://doi.org/10.1016/j.wace.2022.100474.

Rosenfeld, D., 1987: Objective method for analysis and tracking of convective cells as seen by radar. *J. Atmos. Oceanic Technol.*, **4**, 422–434, https://doi.org/10.1175/1520-0426(1987)004<0422:OMFAAT>2.0.CO;2.

Scharfenberg, K. A., 2003: Polarimetric radar signatures in microburst-producing thunderstorms. *31st International Conference on Radar Meteorology*, Seattle, WA, American Meteorological Society, 581–584.

Smith, T. M., K. L. Elmore, and S. A. Dulin, 2004: A damaging downburst prediction and detection algorithm for the WSR-88D. *Wea. Forecasting*, **19**, 240–250, https://doi.org/10.1175/1520-0434(2004)019<0240:ADDPAD>2.0.CO;2.

Snyder, J. C., A. V. Ryzhkov, M. R. Kumjian, A. P. Khain, and J. Picca, 2015: A Z_{DR} column detection algorithm to examine convective storm updrafts. *Wea. Forecasting*, **30**, 1819–1844, https://doi.org/10.1175/WAF-D-15-0068.1.

Srivastava, R. C., 1985: A simple model of evaporatively driven downdraft: application to microburst downdraft. *J. Atmos. Sci.*, **42 (10)**, 1004–1023, https://doi.org/10.1175/1520-0469(1985)042<1004:ASMOED>2.0.CO;2.

———, R. C., 1987: A model of intense downdrafts driven by the melting and evaporation of precipitation. *J. Atmos. Sci.*, **44 (13)**, 1752–1774, https://doi.org/10.1175/1520-0469(1987)044<1752:AMOIDD>2.0.CO;2.

Suzuki, S., T. Maesaka, K. Iwanami, R. Misumi, S. Shimizu, and M. Maki, 2010: Multi-parameter radar observation of a downburst storm in Tokyo on 12 July 2008. *SOLA*, **6**, 53–56, https://doi.org/10.2151/sola.2010-014.

Trapp, R. J., D. M. Wheatley, N. T. Atkins, R. W. Przybylinski, and R. Wolf, 2006: Buyer beware: some words of caution on the use of severe wind reports in postevent assessment and research. *Wea. Forecasting*, **21**, 408–415, https://doi.org/10.1175/WAF925.1.

Vasiloff, S. V., and K. W. Howard, 2009: Investigation of a severe downburst storm near Phoenix, Arizona, as seen by a mobile doppler radar and the KIWA WSR-88D. *Wea. Forecasting*, **24**, 856–867, https://doi.org/10.1175/2008WAF2222117.1.

Vulpiani, G., M. Montopoli, L. D. Passeri, A. G. Gioia, P. Giordano, and F. S. Marzano, 2012: On the use of dual-polarized C-band radar for operational rainfall retrieval in mountainous areas. *J. Appl. Meteor. Climatol.*, **51**, 405–425, https://doi.org/10.1175/JAMC-D-10-05024.1.

Wakimoto, R. M., 1985: Forecasting dry microburst activity over the high plains. *Mon. Wea. Rev.*, **113**, 1131–1143, https://doi.org/10.1175/1520-0493(1985)113<1131:FDMAOT>2.0.CO;2.

———, R. M., and V. N. Bringi, 1988: dual-polarization observations of microbursts associated with intense convection: The 20 July storm during the MIST project. *Mon. Wea. Rev.*, **116**, 1521–1539, https://doi.org/10.1175/1520-0493(1988)116<1521:DPOOMA>2.0.CO;2.

Wang, H., V. Chandrasekar, J. He, Z. Shi, and L. Wang, 2018: Characteristic analysis of the downburst in Greely, Colorado on 30 July 2017 using WPEA method and X-Band radar observations. *Atmosphere*, **9**, 348, https://doi.org/10.3390/atmos9090348.

Wilson, J. W., R. D. Roberts, C. Kessinger, and J. McCarthy, 1984: Microburst wind structure and evaluation of doppler radar for airport wind shear detection. *J. Appl. Meteor. Climatol.*, **23**, 898–915, https://doi.org/10.1175/1520-0450(1984)023<0898:MWSAEO>2.0.CO;2.

Wolfson, M. M., J. T. DiStefano, and T. T. Fujita, 1985: Low-altitude wind shear characteristics in the Memphis, TN area based on Mesonet and LLWAS data. *14th Conference on Severe Local Storms*, Boston, MA, American Meteorological Society, 322–327.